

## Revision 1

# Probing transformation path from aluminum (oxy)hydroxides (boehmite, bayerite, and gibbsite) to metastable alumina: A view from high-resolution $^{27}\text{Al}$ MAS NMR

1 **Hyo-Im Kim<sup>1</sup>, Sung Keun Lee<sup>1,2\*</sup>**

2

3 <sup>1</sup>School of Earth and Environmental Sciences, Seoul National University, Seoul, Korea

4 <sup>2</sup>Institute of Applied Physics, Seoul National University, Seoul, Korea

5

6

7

8

9

10

11

12

13

14

15

16 \*Corresponding author

17 Sung Keun Lee

18 Professor

19 School of Earth and Environmental Sciences

20 Seoul National University, Seoul, 08826, Republic of Korea

21 E-mail: [sunglee@snu.ac.kr](mailto:sunglee@snu.ac.kr)

22 Webpage: <http://hosting03.snu.ac.kr/~sunglee>

23 Phone: 82-2-880-6729

24

25

26 Revised version submitted to "American Mineralogist"

27 June-19-2020

Kim and Lee

## Abstract

28  
29  
30  
31  
32  
33  
34  
35  
36  
37  
38  
39  
40  
41  
42  
43  
44  
45  
46  
47  
48  
49  
50  
51  
52  
53  
54  
55  
56  
57

Detailed knowledge of the structural evolution of diverse aluminum (oxy)hydroxides with varying temperatures up to  $\sim 300$  °C provides insights into the dehydration processes involving transitions among *metastable* phases in Earth's surface and crust. Here, we report the high-resolution solid-state  $^{27}\text{Al}$  NMR spectra for three different types of aluminum (oxy)hydroxides (i.e., boehmite, bayerite, and gibbsite) with varying annealing temperatures up to 300 °C, revealing the effect of distinct precursor minerals on the stability of metastable alumina.  $^{27}\text{Al}$  MAS NMR results allow us to obtain the quantitative fractions and NMR parameters for each phase during transformation. The results demonstrate that each aluminum (oxy)hydroxide phase follows the unique transformation path to metastable alumina. The  $^{27}\text{Al}$  MAS and 3QMAS NMR spectra of boehmite show that a minor but observable  $^{41}\text{Al}$  signal ( $\sim 2\%$ ) is detected at  $\sim 50$  °C, and the  $^{41}\text{Al}$  fraction gradually increases up to 300 °C ( $\sim 16\%$ ), indicating that the phase transformation from boehmite to  $\gamma$ -/ $\eta$ - $\text{Al}_2\text{O}_3$  occurs at a temperature as low as  $\sim 50$  °C, significantly lower than earlier estimations based on XRD. Together with the  $^{41}\text{Al}$  fraction, the  $^{51}\text{Al}$  fraction increases from  $< 1\%$  at 50 °C to  $\sim 2.3\%$  at 300 °C, whereas the NMR results of bayerite and gibbsite do not show the presence of  $^{51}\text{Al}$ . In addition, the  $^{27}\text{Al}$  3QMAS NMR spectra resolved the  $^{61}\text{Al}$  site in boehmite and that in  $\gamma$ -/ $\eta$ - $\text{Al}_2\text{O}_3$ , which could not be uniquely determined from 1D NMR spectra. The population of bayerite abruptly decreases from 100% (at 150 °C), through  $\sim 47\%$  (at 200 °C), to 0% (at 250 °C), indicating that the phase transition from bayerite to boehmite +  $\gamma$ -/ $\eta$ - $\text{Al}_2\text{O}_3$  occurs within a narrow temperature range. As for gibbsite, while  $^{41}\text{Al}$  is not observed in the spectra up to 200 °C, the  $^{41}\text{Al}$  fraction of  $\sim 2\%$  is observed in the spectra for gibbsite annealed at 250 °C, and the  $^{41}\text{Al}$  fraction increases rapidly to  $\sim 15\%$  as the annealing temperature increases to 300 °C, suggesting that the phase transformation into  $\gamma$ -/ $\eta$ - $\text{Al}_2\text{O}_3$  occurs at  $\sim 250$  °C. The results confirm that the phase transformation paths (gradual *vs.* dramatic) depend on the type of precursor minerals. Particularly, the threshold temperature at which the onset of the phase transformation from boehmite to metastable alumina ( $\sim 50$  °C) is lower than those from other precursor minerals ( $> 150$  °C). Furthermore, the phase transformation from boehmite to  $\gamma$ -/ $\eta$ - $\text{Al}_2\text{O}_3$  occurs gradually within broad temperature ranges from  $\sim 50$  °C. This is due to

Kim and Lee

58 their configurational disorder as evidenced by the presence of  $^{[5]}Al$ . The observed structural  
59 evolution in aluminum (oxy)hydroxides in the low-temperature range facilitates the  
60 understanding of the nature of phase transformation and dehydration of oxides and  
61 hydroxides on the Earth's surface environments.

62

63 **Keywords:** Metastable (transition) alumina, aluminum (oxy)hydroxide, solid-state NMR,  $\gamma$ -  
64  $\eta$ - $Al_2O_3$ , phase transformation, extent of disorder

65

66

67

### Introduction

68 The aluminum (oxy)hydroxides and aluminum oxides (i.e., alumina) exist in various  
69 stable and metastable polymorphs in the Earth's surface environments. Particularly,  
70 bauxite, which is the primary ore source of aluminum, consists of diverse types of  
71 aluminum (oxy)hydroxides, such as boehmite and gibbsite (e.g., Kloprogge et al., 2006;  
72 Radusinović et al., 2017 and references therein). In addition, the various forms of metastable  
73 aluminum (oxy)hydroxides [e.g., pseudoboehmite and amorphous  $Al(OH)_3$ ] are found in  
74 the precipitates in acid mine drainage (e.g., Jones et al., 2011; Kim, 2015). The dehydration  
75 (and dehydroxylation) of aluminum (oxy)hydroxides (i.e., gibbsite and boehmite) in natural  
76 bauxite occurs at 200-300 °C (e.g., Kloprogge et al., 2002), which corresponds to the  
77 temperature range of diagenesis. Although it is difficult to identify the metastable  $Al_2O_3$  in  
78 natural bauxite due to their poor crystallinity, earlier studies have reported the presence of  
79  $\eta$ - $Al_2O_3$  and hydrated- $Al_2O_3$  [i.e., akdalaite ( $5Al_2O_3 \cdot H_2O$ )] in natural bauxite (e.g., Tilley and  
80 Eggleton, 1996; Hwang et al., 2006).

81 Aluminum oxides also exist in diverse metastable polymorphs, called transition  
82 alumina (such as  $\gamma$ -,  $\delta$ -,  $\theta$ -,  $\kappa$ -,  $\chi$ -, and  $\eta$ - $Al_2O_3$ ), and stable  $\alpha$ - $Al_2O_3$ . Metastable aluminas  
83 have diverse industrial applications such as catalyst supports, absorbents, and protective  
84 barriers to prevent corrosion on alumina-forming alloys, because of their high surface area  
85 and the high catalytic activity at their surfaces (e.g., Che and Bennett, 1989; Cai et al., 2003  
86 and references therein). Extensive experimental and theoretical studies have revealed the  
87 structures and catalytic properties of metastable aluminas (e.g., John et al., 1983; Krokidis et

Kim and Lee

88 al., 2001; Sohlberg et al., 2001; Cai et al., 2002; Paglia et al., 2003; Alphonse and Courty, 2005;  
89 Paglia et al., 2006; Kwak et al., 2008; Boumaza et al., 2009; Kim and Lee, 2013b). Metastable  
90 aluminas can be obtained by the heat treatments of various aluminum (oxy)hydroxides  
91 precursors, such as boehmite ( $\gamma$ -AlOOH), bayerite [ $\alpha$ -Al(OH)<sub>3</sub>], and gibbsite [ $\gamma$ -Al(OH)<sub>3</sub>].  
92 Figure 1 shows the crystal structures for three different types of aluminum (oxy)hydroxides  
93 and  $\gamma$ -Al<sub>2</sub>O<sub>3</sub>. The crystallographic information of aluminum (oxy)hydroxide precursors (i.e.,  
94 boehmite, bayerite, and gibbsite) and metastable alumina (i.e.,  $\gamma$ - and  $\eta$ -Al<sub>2</sub>O<sub>3</sub>) are shown in  
95 Table 1 (Hill, 1981; Balan et al., 2006; Balan et al., 2008).

96 The phase transformation paths from aluminum (oxy)hydroxides to stable  $\alpha$ -Al<sub>2</sub>O<sub>3</sub>  
97 via metastable aluminas have been extensively explored (e.g., Levin and Brandon, 1998;  
98 Digne et al., 2002; Chandran et al., 2019 and references therein). The transformation  
99 temperatures are also affected by various factors such as particle size (IngramJones et al.,  
100 1996; Tsukada et al., 1999; Bokhimi et al., 2007; Kim and Lee, 2013b), morphology (Lee et al.,  
101 2015; Karouia et al., 2016), and synthesis conditions (Kim et al., 2005; Chen et al., 2018).  
102 Briefly, the annealing of boehmite ( $\gamma$ -AlOOH) produces the series of metastable alumina of  
103  $\gamma$ - (~300-500 °C),  $\delta$ - (~700-800 °C), and  $\theta$ -Al<sub>2</sub>O<sub>3</sub> (900-1000 °C), and then stable  $\alpha$ -Al<sub>2</sub>O<sub>3</sub> (1000-  
104 1100 °C) (e.g., Levin and Brandon, 1998; Chagas et al., 2014). Bayerite [ $\alpha$ -Al(OH)<sub>3</sub>]  
105 transforms into  $\alpha$ -Al<sub>2</sub>O<sub>3</sub> via  $\eta$ - (200-300 °C) and  $\theta$ -Al<sub>2</sub>O<sub>3</sub> (600-800 °C), or via boehmite  
106 (~150 °C),  $\gamma$ - (300-450 °C),  $\delta$ - (~700-800 °C), and  $\theta$ -Al<sub>2</sub>O<sub>3</sub> (900-1000 °C) (e.g., Pecharroman et  
107 al., 1999; Digne et al., 2002). The transformation to boehmite from bayerite is reported to  
108 occur above 150 °C with a fast heating rate (above 2 °C/min) (e.g., Maruthiprasad et al.,  
109 1988; Kim et al., 2005). As for gibbsite [ $\gamma$ -Al(OH)<sub>3</sub>], the transformation sequence follows two  
110 paths depending on the particle size and water contents (e.g., Rouquerol et al., 1975;  
111 Mercury et al., 2006). Coarse gibbsite (i.e., > ~10  $\mu$ m) with excess water content generally  
112 transforms to boehmite at ~200 °C (IngramJones et al., 1996; Hill et al., 2007; Chen et al.,  
113 2018). The annealing of fine gibbsite (~0.5  $\mu$ m) under a dry condition follows the sequence  
114 of  $\chi$ - (150-300 °C),  $\kappa$ - (650-750 °C), and  $\alpha$ -Al<sub>2</sub>O<sub>3</sub> (~1000 °C) (Brindley and Choe, 1961;  
115 IngramJones et al., 1996). The phase transformation occurs over a broad temperature range  
116 rather than at a well-defined single temperature due to the pronounced metastability (see  
117 Levin and Brandon, 1998; Kim and Lee, 2013b; Chandran et al., 2019 and references therein).

Kim and Lee

118 Furthermore, the metastability results in the coexistence of two or more phases at the same  
119 temperature.

120 Diverse experimental techniques such as differential thermal analysis (DTA),  
121 infrared (IR) spectroscopy, X-ray diffraction (XRD), and solid-state nuclear magnetic  
122 resonance (NMR) have observed phase transformation from aluminum (oxy)hydroxides  
123 into metastable aluminas (e.g., Bastow et al., 1994; Tsukada et al., 1999; Alphonse and  
124 Courty, 2005; Karouia et al., 2016; Chen et al., 2018; Chandran et al., 2019). In particular, <sup>27</sup>Al  
125 NMR has revealed the Al coordination environments in diverse disordered crystalline (i.e.,  
126 metastable)/amorphous Al<sub>2</sub>O<sub>3</sub> and Al-(oxy)hydroxides (e.g., Lippmaa et al., 1986; Lee et al.,  
127 2003; Boissiere et al., 2006; Shen et al., 2007; Lee et al., 2009b; Lee et al., 2010; Sabarinathan et  
128 al., 2010; Kim and Lee, 2013b; Cui et al., 2018; Lee and Ryu, 2018; He et al., 2019 and  
129 references therein). The Al coordination environments and the NMR parameters, including  
130 quadrupolar coupling constant ( $C_q$ ), isotropic chemical shifts ( $\delta_{iso}$ ), and asymmetry  
131 parameter ( $\eta$ ) for aluminum (oxy)hydroxides and metastable aluminas from these earlier  
132 studies are summarized in Table 2. Whereas a presence of a small amount of metastable  
133 alumina is often difficult to identify via XRD, earlier <sup>27</sup>Al NMR results enable quantification  
134 of the fractions of coexisting phases in the transition aluminas and aluminum  
135 (oxy)hydroxides from the simulation of NMR spectra, even though the fraction of the minor  
136 phase is very small percentage. (Pecharroman et al., 1999; O'Dell et al., 2007; Kwak et al.,  
137 2008; Kim and Lee, 2013b; Chagas et al., 2014; Chandran et al., 2019). We also showed that  
138 the particle size and structural disorder in metastable alumina nanoparticles significantly  
139 affects their thermal stability above 600 °C (Kim and Lee, 2013b).

140 Despite the geochemical implications and industrial applications, the precise  
141 determination of the short-range structure and stability (e.g., temperature conditions) of  
142 metastable aluminas in the low-temperature range (< 300 °C) remains challenging.  
143 Particularly, the transformation temperatures at which the formation of metastable alumina  
144 from diverse aluminum (oxy)hydroxides occurs remain to be determined. A systematic  
145 study of the changes in the Al coordination number with varying temperatures below  
146 300 °C would therefore provide mechanistic details of the low-temperature surface  
147 processes. In this study, we investigated the dehydration paths to metastable alumina from

Kim and Lee

148 various aluminum (oxy)hydroxide precursors (i.e., boehmite, bayerite, and gibbsite) in the  
149 low-temperature range up to 300 °C using high-resolution  $^{27}\text{Al}$  MAS and 3QMAS NMR. We  
150 explored the effect of aluminum (oxy)hydroxide precursors (i.e., boehmite, bayerite, and  
151 gibbsite) on the stability of metastable alumina below 300 °C. Based on our spectroscopic  
152 results in the low-temperature range, we discuss the importance of the structural findings  
153 in understanding the geological (dehydration) processes involving metastable phase  
154 transformation on the Earth's surface environments.

155

156

### Materials and methods

157 **Sample preparation.** Boehmite ( $\gamma\text{-AlOOH}$ ) and bayerite [ $\alpha\text{-Al(OH)}_3$ ] were synthesized by  
158 hydrolysis of aluminum tri-*sec*-butoxide (ASB, Sigma Aldrich, product no. 2269-22-9). The  
159 type of precursor synthesized depends on the amount of water used for hydrolysis of  
160 ASB (e.g., Serna et al., 1977; Vaudry et al., 1996). Particularly, boehmite is formed by the  
161 hydrolysis of ASB with  $\text{H}_2\text{O}/\text{Al}$  of  $\sim 3$ , while the hydrolysis with the higher amount of  
162 excess water (i.e.,  $\text{H}_2\text{O}/\text{Al} > 20$ ) results in the formation of bayerite. Boehmite was  
163 prepared by adding 4.52 g of aluminum tri-*sec*-butoxide to 1.04 mL of distilled water. The  
164 mixture was dried for a week at 25 °C in air. Bayerite was synthesized from a mixture of  
165 5.23 g of aluminum tri-*sec*-butoxide with 200 mL of distilled water, which was dried at  
166 room temperature. Gibbsite [99.7% of  $\gamma\text{-Al(OH)}_3$ ] was obtained from KC Corporation in  
167 Korea and was used as received. The medium value of the particle size distribution ( $D_{50}$ )  
168 for as-received gibbsite is  $\sim 50$   $\mu\text{m}$ . The samples were annealed at varying temperatures in  
169 a vertical tube furnace from 110 °C to 300 °C and in a heating mantle up to 50 °C (2 hours).  
170 The annealing temperature of the samples was increased with the rate of 275 °C/h to the  
171 target temperatures (e.g., 110~300 °C), and further isothermal annealing was performed  
172 for 2 hours. Note that the total heating time (i.e., time to elevate temperature + isothermal  
173 annealing time) slightly varies with the target temperature from 2.5 h for 110 °C to 3 h for  
174 300 °C.

175 **X-ray diffraction.** X-ray diffraction patterns for starting materials (i.e., boehmite, bayerite,  
176 and gibbsite) and heat-treated samples were collected on Rigaku Miniflex 600

Kim and Lee

177 diffractometer using CuK $\alpha$  X-ray (a voltage of 40 kV and a current of 15 mA) with 20  
178 range of 10-80°, step size of 0.02-0.04°, and a scan rate of 1-3 s per point.

179 **NMR spectroscopy.**  $^{27}\text{Al}$  MAS NMR spectra were obtained using a Bruker Avance II 500  
180 MHz NMR system (11.7 T, at Seoul National University) with 4 mm triple-resonance  
181 MAS probe at Larmor frequency of 130.28 MHz. For a series of boehmite,  $^{27}\text{Al}$  NMR  
182 spectra were also obtained with a Varian 600 spectrometer (14.1 T, at Korea Basic Science  
183 Institute) with 2.5 mm double-resonance probe at Larmor frequency of 156.34 MHz.

184 Sample spinning speeds of 15 kHz (11.7 T) and 20 kHz (14.1 T) were used. A single-pulse  
185 sequence with  $\sim 0.2 \mu\text{s}$  ( $\sim 15^\circ$  tip angle for central transition in solids) and delay time of 1 s  
186 were used. The baseline of the collected 1D NMR spectra was fitted by a fourth-order  
187 polynomial function using Topspin 3.5 software, and then, was subtracted from the  
188 obtained spectra for flattening the baseline around central transition peaks ( $\sim 200$  ppm to  
189  $\sim -200$  ppm). The phase of each spectrum was carefully adjusted to optimize the baseline  
190 of the spectra. The simulation of  $^{27}\text{Al}$  MAS NMR spectra was performed with the Dmfit  
191 program (Massiot et al., 2002).  $^{27}\text{Al}$  3QMAS NMR spectra were collected on the Varian  
192 400 MHz (9.4 T) spectrometer with Doty Scientific double-resonance MAS probe and 4  
193 mm thick-wall zirconia rotor. The fast amplitude modulation-based on shifted-echo pulse  
194 sequences comprising two hard pulses (with  $3 \mu\text{s}$  and  $0.7 \mu\text{s}$ ) and, a soft pulse (with  $15 \mu\text{s}$ )  
195 were used. An echo-delay of approximately 0.5 ms (half-integer multiple of the rotor  
196 period) were used with a phase table of 96 cycles, designed to select full echo. The pulse  
197 lengths used in the current sequence are carefully optimized to ensure maximum  
198 intensity. The radio-frequency (*rf*) field strengths for hard pulses for  $^{27}\text{Al}$  3QMAS NMR  
199 are  $\sim 125$  kHz. Approximately 120-200 FIDs (with the 192 number of scans) were collected  
200 to construct the 2D spectra. To achieve the current signal-to-noise ratio,  $\sim 16$  hours of  
201 collection time were required for each spectra. 3QMAS NMR spectra were processed with  
202 a shear transformation, with the isotropic dimension frequencies scaled as described  
203 previously (e.g., Baltisberger et al., 1996; Lee, 2011; Kim and Lee, 2014 and references  
204 therein). The recycle delay of 1 s and spinning speed of 15 kHz were used. All spectra  
205 were referenced to  $\text{AlCl}_3$  (1M) solution.

206

Kim and Lee

## Results and discussion

207

### 208 Transformation from boehmite to $\gamma$ -/ $\eta$ -Al<sub>2</sub>O<sub>3</sub>

209 **XRD results.** Figure 2A shows the XRD patterns of boehmite with varying temperatures  
210 up to 300 °C. The XRD pattern at 25 °C shows the broad diffraction peaks of boehmite,  
211 consistent with previous XRD studies (e.g., MacKenzie et al., 2000; Krokidis et al., 2001;  
212 Boumaza et al., 2009 and references therein). The diffraction patterns do not change much  
213 with annealing temperature up to 250 °C, suggesting that the transformation from  
214 boehmite to metastable Al<sub>2</sub>O<sub>3</sub> at the range of 25-250 °C is not prevalent. In contrast, the  
215 pattern of boehmite annealed at 300 °C revealed the (400) and (440) peaks of metastable  
216 Al<sub>2</sub>O<sub>3</sub> increased, indicating the presence of metastable Al<sub>2</sub>O<sub>3</sub> (i.e.,  $\gamma$ - and/or  $\eta$ -Al<sub>2</sub>O<sub>3</sub>).

217 Note that the XRD patterns of  $\gamma$ -Al<sub>2</sub>O<sub>3</sub> and  $\eta$ -Al<sub>2</sub>O<sub>3</sub> are *almost* identical (Lippens  
218 and De Boer, 1964; Zhou and Snyder, 1991). As shown in Table 1, both  $\gamma$ - and  $\eta$ -Al<sub>2</sub>O<sub>3</sub>  
219 structures are described as defect spinel structures with space group of Fd $\bar{3}$ m (e.g., Levin  
220 and Brandon, 1998). The only difference stems from the variations in the distribution of  
221 vacancy in the cation sites: the vacancy in ideal  $\gamma$ -Al<sub>2</sub>O<sub>3</sub> is located in the tetrahedral sites,  
222 while that in  $\eta$ -Al<sub>2</sub>O<sub>3</sub> appears to favor octahedral sites (e.g., Lippens and De Boer, 1964).  
223 As  $\gamma$ - and  $\eta$ -Al<sub>2</sub>O<sub>3</sub> are not well-distinguished (e.g., Zhou and Snyder, 1991), we refer to  
224 the metastable alumina as  $\gamma$ -/ $\eta$ -Al<sub>2</sub>O<sub>3</sub>. The width of the diffraction patterns of boehmite  
225 at 25 °C is broader than those of bayerite and gibbsite, indicating the low crystallinity  
226 and/or a more pronounced structural disorder in boehmite (see below).

227 **<sup>27</sup>Al NMR results.** Figures 2B and 2C show the <sup>27</sup>Al MAS NMR spectra (11.7 T and 14.1 T)  
228 for synthesized boehmite with varying annealing temperatures up to 300 °C. At 25 °C (as-  
229 synthesized boehmite), the spectrum predominantly shows <sup>6</sup>Al at ~10 ppm, consistent  
230 with previous NMR studies (Bastow et al., 1994; Isobe et al., 2003). Though minor, ~1% of  
231 <sup>4</sup>Al peak at ~68 ppm is observed at 25 °C. As the <sup>4</sup>Al peak is not due to the rotor  
232 background (e.g., Lee et al., 2010; Lee et al., 2016). This may be partly due to the presence of  
233 aluminum (oxy)hydroxide complex with <sup>4</sup>Al, such as Al<sub>13</sub> [i.e., AlO<sub>4</sub>Al<sub>12</sub>(OH)<sub>24</sub>(H<sub>2</sub>O)<sup>7+</sup>]<sub>12</sub>  
234 (e.g., Phillips et al., 2000a; Kim, 2015). In addition, while the boehmite in the current study  
235 was not ground, the earlier studies have reported that the grinding of boehmite can result  
236 in the presence of <sup>[4,5]</sup>Al in boehmite (e.g., Chen et al., 1992; MacKenzie et al., 2000).



Kim and Lee

237 Furthermore, the possible presence of a minor amount of  $\gamma$ -/ $\eta$ - $\text{Al}_2\text{O}_3$  at ambient  
238 temperature may not be fully discarded.

239 As the annealing temperature increases, the  $^{41}\text{Al}$  peak intensity (at  $\sim 70$  ppm)  
240 gradually increases. The  $^{41}\text{Al}$  peak width also increases with increasing annealing  
241 temperature. Particularly, the peak width of  $^{41}\text{Al}$  increases from  $\sim 16$  ppm (for boehmite  
242 annealed at  $50^\circ\text{C}$ ) to  $\sim 22$  ppm (for boehmite annealed at  $300^\circ\text{C}$ ) at 11.7 T, and that  
243 increases from  $\sim 14$  ppm (at  $50^\circ\text{C}$ ) to  $\sim 20$  ppm (at  $300^\circ\text{C}$ ) at 14.1 T (see Figure 3). The  
244 narrower peak widths of Al sites at 14.1 T (than those at 11.7 T) is because the magnitude of  
245 quadrupolar interaction decreases with increasing magnetic fields (e.g., Kohn et al., 1998;  
246 Stebbins et al., 2000 and references therein). The spectra at both fields reveal a small but  
247 noticeable presence of  $^{51}\text{Al}$  (at  $\sim 35$  ppm), and the fraction of  $^{51}\text{Al}$  apparently increases with  
248 increasing annealing temperature. These results indicate that the phase transformation from  
249 boehmite to  $\gamma$ -/ $\eta$ - $\text{Al}_2\text{O}_3$  occurs at a temperature as low as  $\sim 50^\circ\text{C}$ . The presence of small  
250 amounts of  $\gamma$ -/ $\eta$ - $\text{Al}_2\text{O}_3$  below  $300^\circ\text{C}$ , which was observed in high-resolution NMR spectra,  
251 is not revealed in the XRD patterns. Note that, while ideal  $\gamma$ - and  $\eta$ - $\text{Al}_2\text{O}_3$  structures have  
252 different  $^{41}\text{Al}$ : $^{61}\text{Al}$  ratios, it is difficult to distinguish  $\gamma$ - and  $\eta$ - $\text{Al}_2\text{O}_3$  in the NMR spectra and  
253 these phases often coexist (Lippens and De Boer, 1964; Damodaran et al., 2002; Digne et al.,  
254 2002; Chandran et al., 2019).

255

### 256 **Transformation from bayerite to boehmite + $\gamma$ -/ $\eta$ - $\text{Al}_2\text{O}_3$**

257 **XRD results.** Figure 4A shows the XRD patterns for bayerite with varying annealing  
258 temperatures up to  $300^\circ\text{C}$ . The width of the main diffraction peaks [i.e., (002) peak] for  
259 bayerite at  $25^\circ\text{C}$  ( $\sim 0.2^\circ$ ) is significantly narrower than that for boehmite at  $25^\circ\text{C}$  ( $\sim 5^\circ$ ),  
260 indicating that the crystallinity of bayerite is higher than that of boehmite. As shown in  
261 Figure 4A, there are no significant changes in the XRD patterns with increasing  
262 temperature for bayerite up to  $200^\circ\text{C}$ . However, for the bayerite annealed at  $250^\circ\text{C}$ , the  
263 diffraction patterns of bayerite abruptly disappear. Instead, patterns of both boehmite  
264 and metastable alumina are observed. The XRD results confirm that the bayerite  
265 transformed into boehmite and metastable  $\text{Al}_2\text{O}_3$  (i.e.,  $\gamma$ -/ $\eta$ - $\text{Al}_2\text{O}_3$ ) above  $\sim 250^\circ\text{C}$ ,  
266 consistent with previous studies (Zhou and Snyder, 1991; Digne et al., 2002).

Kim and Lee

267 **<sup>27</sup>Al NMR results.** Figures 4B-D present the <sup>27</sup>Al MAS NMR spectra at 11.7 T of bayerite  
268 with varying annealing temperatures up to 300 °C, showing the evolution of Al sites due  
269 to the phase transformation of bayerite to boehmite + metastable  $\gamma$ -/ $\eta$ -Al<sub>2</sub>O<sub>3</sub>. For the  
270 spectra of bayerite at 25 °C, the asymmetric shape of <sup>6</sup>Al peak (with peak maximum at  
271 ~11.4 ppm) is observed. The <sup>6</sup>Al peak shape with a shoulder at ~8 ppm may be due to  
272 two crystallographic inequivalent <sup>6</sup>Al sites, consistent with the previous NMR study  
273 (Bastow et al., 1994). The previously reported NMR parameters for bayerite are shown in  
274 Table 2 (Damodaran et al., 2002). As shown in Figure 4B, only <sup>6</sup>Al peak is observed in  
275 the spectra for annealed bayerite up to 150 °C. A noticeable fraction of <sup>4</sup>Al sites is  
276 observed in the spectra for bayerite annealed at 200 °C, and the fraction of <sup>4</sup>Al increases  
277 with increasing temperature from 200 °C to 300 °C. Though the difference is minor, the  
278 <sup>6</sup>Al peak width increases with increasing temperature from ~7 ppm (at 150 °C) to ~8  
279 ppm (at 200 °C), suggesting the increase in the fraction of disordered phase (i.e.,  
280 metastable alumina) with increasing temperature. In addition, the peak shape evolves  
281 with the long tails extending lower frequency due to larger extent of distribution of C<sub>q</sub>  
282 above 200 °C. These results indicate that the phase transformation from bayerite to  $\gamma$ -/ $\eta$ -  
283 Al<sub>2</sub>O<sub>3</sub> occurs at ~200 °C. We also note that the presence of  $\gamma$ -/ $\eta$ -Al<sub>2</sub>O<sub>3</sub> is not observed in  
284 the XRD pattern at 200 °C (Figure 4A). The <sup>5</sup>Al sites are not observed in the spectra of  
285 the bayerite series, even at 300 °C (Figure 4C), in contrast to the results of the boehmite  
286 series. Furthermore, the peak widths of <sup>4</sup>Al and <sup>6</sup>Al of the spectra of the phases formed  
287 from bayerite at 300 °C appears to be wider than those formed from the boehmite  
288 precursor at 300 °C (Figure 2B), suggesting a larger fraction of metastable alumina in the  
289 former (see below for the quantification of phases).

290

### 291 **Transformation from gibbsite to boehmite + $\gamma$ -/ $\eta$ -Al<sub>2</sub>O<sub>3</sub>**

292 **XRD results.** In the XRD patterns of the gibbsite series (Figure 5A), it is observed that the  
293 phase transformation from gibbsite to boehmite with increasing temperature occurs from  
294 ~200 °C. The intensity of the XRD pattern for boehmite gradually increases with  
295 increasing temperature from 200 °C to 300 °C. The XRD pattern for the gibbsite annealed  
296 at 300 °C shows that gibbsite is completely transformed into boehmite. Note that the peak

Kim and Lee

297 width of gibbsite-derived boehmite (at 200 °C) is narrower than that of annealed  
298 boehmite formed from sol-gel synthesis at 200 °C, suggesting the higher crystallinity in  
299 the former. Though minor, the broad diffraction peaks of metastable-Al<sub>2</sub>O<sub>3</sub> (at the 2θ of  
300 ~37°, ~43°, and 66°) are observed in the pattern of heat-treated gibbsite at 300 °C.  
301 However, for gibbsite annealed at 250 °C, the presence of γ-/η-Al<sub>2</sub>O<sub>3</sub> is not confirmed in  
302 the current XRD pattern.

303 **<sup>27</sup>Al NMR results.** Figures 5B-D show the <sup>27</sup>Al MAS NMR spectra at 11.7 T for gibbsite  
304 with varying annealing temperatures. The spectra at 25 °C show two crystallographically  
305 distinct <sup>6</sup>Al sites (Bastow et al., 1994; Hill et al., 2007). See Table 2 for detailed  
306 information on the previously reported NMR parameters for two different <sup>6</sup>Al sites.  
307 Above 200 °C, the spectra show subtle and gradual changes in the peak shape of <sup>6</sup>Al,  
308 suggesting the phase transformation to boehmite. At 250 °C, the <sup>4</sup>Al peak is observed,  
309 and the peak intensity of <sup>4</sup>Al increases with increasing temperature (Figure 5D).

310 Although the presence of γ-/η-Al<sub>2</sub>O<sub>3</sub> at 250 °C is not observed in the XRD patterns, the  
311 presence of <sup>4</sup>Al peak in the NMR spectra at 250 °C confirms the formation of γ-/η-Al<sub>2</sub>O<sub>3</sub>.  
312 This indicates that XRD alone may not reveal the presence of minor amount of structural  
313 disordered (or poorly crystalline) metastable Al<sub>2</sub>O<sub>3</sub> phases. The <sup>5</sup>Al peak in the heat-  
314 treated gibbsite is not evident in the NMR spectra, while the presence of <sup>5</sup>Al is observed  
315 in the heat-treated boehmite (see discussion below).

316

### 317 **<sup>27</sup>Al 3QMAS NMR results for boehmite with varying temperature**

318 In addition to structural insights from 1D MAS NMR spectra (Figures 2-5), 2D  
319 3QMAS NMR spectra for the samples allow us to trace the detailed changes in the  
320 populations of phases involving transformation. Figure 6 shows the <sup>27</sup>Al 3QMAS NMR  
321 spectra for boehmite before and after annealing at 110, 200, and 300 °C for 2 h, providing  
322 enhanced resolution among Al sites. By achieving the current signal-to-noise ratio, a minor  
323 fraction of <sup>4,5</sup>Al sites can be resolved in the current 2D NMR spectra. Note that the noise  
324 overlapping the signal of <sup>n</sup>Al was not observed on the 1% contour lines [see Supplemental  
325 Materials 1 (SI-1)]. In addition, the overlap between the signals and spinning sideband was  
326 not observed in the current spectra. The <sup>6</sup>Al peak at ~-10 ppm in the isotropic dimension is

Kim and Lee

327 observed at 25 °C. As the temperature increases from 110 °C to 300 °C, the  $^{51}\text{Al}$  peak at  $\sim$ -28  
328 ppm and  $^{41}\text{Al}$  peak at  $\sim$ -45 ppm in the isotropic dimension apparently increase (e.g.,  
329 Baltisberger et al., 1996; Stebbins et al., 2000; Lee et al., 2009b). The increase in the intensities  
330 of  $^{4,51}\text{Al}$  sites indicates that phase transformation of boehmite  $\rightarrow$   $\gamma$ -/ $\eta$ - $\text{Al}_2\text{O}_3$  occurs  
331 gradually within a broad temperature ranges. These results are consistent with those of the  
332  $^{27}\text{Al}$  MAS NMR spectra (Figure 3).

333 Figure 7 shows the changes in  $^{61}\text{Al}$  increasing annealing temperature resulting from  
334 the variations in the relative fractions between boehmite and  $\gamma$ -/ $\eta$ - $\text{Al}_2\text{O}_3$ . The 2D NMR  
335 spectra resolved the  $^{61}\text{Al}$  site in boehmite and that in  $\gamma$ -/ $\eta$ - $\text{Al}_2\text{O}_3$ , which could not be  
336 uniquely determined from 1D NMR spectra. The expected position of  $^{61}\text{Al}$  peak in boehmite  
337 and  $\gamma$ -/ $\eta$ - $\text{Al}_2\text{O}_3$  can be estimated from the NMR parameters shown in Table 2 (Kraus et al.,  
338 1996; Pecharroman et al., 1999; Perander et al., 2007; Kim and Lee, 2013b) and currently  
339 estimated parameters from simulation of  $^{27}\text{Al}$  MAS NMR spectra (Table 3). These are  
340 marked in the  $^{27}\text{Al}$  3QMAS NMR spectra (Figure 7) where the evolution of the shape of  $^{61}\text{Al}$   
341 peaks with varying annealing temperature are highlighted. These changes confirm that the  
342 onset of the phase transformation boehmite  $\rightarrow$   $\gamma$ -/ $\eta$ - $\text{Al}_2\text{O}_3$  is evident at the temperature  
343 lower than the expected ( $< 300$  °C).

344

### 345 **Quantification of coexisting phases in the heat-treated aluminum (oxy)hydroxides**

346 **Quantification protocols.** Because the unique peak shapes of Al sites in aluminum  
347 (oxy)hydroxides and metastable alumina (due to their characteristic NMR parameters)  
348 allows us to deconvolute (and simulate) the NMR spectra, the fraction of consisting  
349 phases in the heat-treated samples was estimated from the NMR spectra (Figures 8-10).  
350 To simulate the NMR spectra for highly-ordered crystalline phases (i.e., bayerite and  
351 gibbsite), Q-mas 1/2 model in Dmfit software was used (e.g., Massiot et al., 2002; Lee et  
352 al., 2009a; Park and Lee, 2019). In the current study, we simulated the bayerite and  
353 gibbsite using well-established values of NMR parameters previously obtained by 2D  
354 NMR. While the slight variation stems from the adjustment to match among  
355 experimental and simulated spectra, the NMR parameters were well-reproduced within  
356 the error range. The spectra for boehmite and metastable alumina were fitted (using

Kim and Lee

357 DMFIT software) using a Gaussian isotropic model distribution (GIM, case of  $d = 5$  of the  
358 more general Czjzek distribution) which assumes a statistical distribution of charges  
359 around the observed nuclei (see references Le Caer and Brand, 1998; Neuville et al., 2004;  
360 Lee et al., 2009a; Kim and Lee, 2013b for more detailed discussion on GIM and the  
361 detailed parameterization to simulate the quadrupolar line shape with disorder and thus  
362 the distribution of electronic field gradient tensors) (see SI-2 for details of simulation  
363 using Dmfit).

364 In the current study, following protocol has been used to estimate the population  
365 of aluminum (oxy)hydroxides and metastable alumina at varying temperature. First, the  
366  $^{27}\text{Al}$  NMR spectra were simulated using the NMR parameters reported in the previous  
367 studies (Pecharroman et al., 1999; Damodaran et al., 2002; Vyalikh et al., 2010; see Table 2;  
368 Kim and Lee, 2013b). Then, these parameters are slightly adjusted to better reproduce the  
369 overall spectra. Second, the constraints on the relative ratio between Al sites for each  
370 phase were applied: boehmite is composed of a single disordered  $^{6}\text{Al}$  site (Damodaran et  
371 al., 2002), and bayerite and gibbsite have two crystallographic inequivalent  $^{6}\text{Al}$  sites with  
372 a ratio of 1:1 (Bastow et al., 1994; Damodaran et al., 2002; Vyalikh et al., 2010). For the  
373 ideal structure of  $\gamma$ - and  $\eta$ - $\text{Al}_2\text{O}_3$ , the  $^{4}\text{Al}$ : $^{6}\text{Al}$  ratios are 25:75 and 38:62, respectively, as  
374 shown in Table 1 (John et al., 1983; Zhou and Snyder, 1991). However, the ratio of  $^{4}\text{Al}$   
375 and  $^{6}\text{Al}$  of  $\gamma$ - and  $\eta$ - $\text{Al}_2\text{O}_3$  of the defected cubic (spinel) structure varies depending on the  
376 distribution of defects on the Al sites (Levin and Brandon, 1998). In addition, it is difficult  
377 to obtain pure  $\gamma$ - and/or  $\eta$ - $\text{Al}_2\text{O}_3$  phases from precursors (Lippens and De Boer, 1964;  
378 Digne et al., 2002). Practically, the earlier NMR studies have shown that the  $^{4}\text{Al}$  and  $^{6}\text{Al}$   
379 fractions in model  $\gamma$ - and  $\eta$ - $\text{Al}_2\text{O}_3$  are ~30% and ~70%, respectively (Pecharroman et al.,  
380 1999; Kim and Lee, 2013b; Chandran et al., 2019). The reported  $^{4}\text{Al}$  and  $^{6}\text{Al}$  ratios are in  
381 between those for ideal structures of  $\gamma$ - (i.e.,  $^{4}\text{Al}$ : $^{6}\text{Al}$  = 25:75) and/or  $\eta$ - $\text{Al}_2\text{O}_3$  (i.e.,  
382  $^{4}\text{Al}$ : $^{6}\text{Al}$  = 38:62). This suggests that  $\gamma$ - and  $\eta$ - $\text{Al}_2\text{O}_3$  often coexist. Thus, in the current  
383 study, the  $^{4}\text{Al}$ : $^{6}\text{Al}$  ratios for  $\gamma$ -/ $\eta$ - $\text{Al}_2\text{O}_3$  were constrained to be 3:7.

384 With the constraint of the intensity ratio of  $^{4}\text{Al}$  and  $^{6}\text{Al}$  for  $\gamma$ -/ $\eta$ - $\text{Al}_2\text{O}_3$ , the  
385 fractions of precursors and the coexisting  $\gamma$ -/ $\eta$ - $\text{Al}_2\text{O}_3$  were estimated (see below). As the  
386 presence of  $^{4}\text{Al}$  is exclusively accompanied with the metastable alumina, the fractions of

Kim and Lee

387 metastable alumina were obtained by the sum of  $^{4}\text{Al}$  and the corresponding  $^{6}\text{Al}$   
388 (i.e.,  $X_{^{6}\text{Al}}^{\gamma\text{-}/\eta\text{-Al}_2\text{O}_3} = 7/3 * X_{^{4}\text{Al}}$ ). The remaining  $^{6}\text{Al}$  intensity (e.g., total  $X_{^{6}\text{Al}} - 7/3 * X_{^{4}\text{Al}}$ ) is  
389 thus attributed to the fraction of aluminum (oxy)hydroxide precursors, because the NMR  
390 peak area directly represents the fraction of phase: for example, the boehmite annealed at  
391 300 °C contains the  $16\pm 3\%$ ,  $3\pm 3\%$ , and  $36\pm 3\%$  of  $^{4}\text{Al}$ ,  $^{5}\text{Al}$ , and  $^{6}\text{Al}$  for  $\gamma\text{-}/\eta\text{-Al}_2\text{O}_3$ ,  
392 respectively, indicating that there are ~55% of  $\gamma\text{-}/\eta\text{-Al}_2\text{O}_3$  and ~45% of boehmite in the  
393 sample. The NMR parameters were allowed to vary slightly depending on the annealing  
394 temperature. The estimated NMR parameters and the fractions for Al sites of each phase  
395 at varying annealing temperature were shown in Tables 3-5. Note that the fraction of  $^{6}\text{Al}$   
396 site for each phase shown in Tables 3-5 was obtained by calculating the ratio of the area  
397 under the  $^{6}\text{Al}$  for the specific phase to the total area in the  $^{27}\text{Al}$  MAS NMR spectra. The  
398 current NMR spectra were also simulated by considering the intensity of spinning  
399 sideband stemming from the satellite transition (see SI-3 for details). Taking into  
400 consideration the minor difference in the estimated fractions of each phase at given  
401 temperature between simulation results with considering and without considering the  
402 spinning sidebands (~1.5%), the contribution of satellite transition to quantification of the  
403 relative fraction between Al sites is rather minor.

404 **Phase transformation from boehmite precursor.** Figures 8 and 9 show the simulated  $^{27}\text{Al}$   
405 MAS NMR spectra at 11.7 T and 14.1 T using identical NMR parameters. Despite the  
406 overlap, the  $^{6}\text{Al}$  peak for  $\gamma\text{-}/\eta\text{-Al}_2\text{O}_3$  and that from boehmite can be partly distinguished.  
407 This is because of the higher  $C_q$  for  $^{6}\text{Al}$  of  $\gamma\text{-}/\eta\text{-Al}_2\text{O}_3$  (~4.8 MHz) than that of boehmite  
408 (~2.7 MHz). Note that reported  $C_q$  values for  $^{6}\text{Al}$  of boehmite varies from 1.8 MHz to 2.8  
409 MHz (Damodaran et al., 2002; Chandran et al., 2019). The  $\delta_{\text{iso}}$  of boehmite in the current  
410 study (~10.8 ppm) is somewhat different from that reported previously between the  
411 previous study (~12.6 ppm) (Damodaran et al., 2002). This because the NMR parameters  
412 in the current study were obtained by simulation of 1D NMR spectra using Czjzek model.  
413 In contrast, those in the previous study were obtained from center of gravity of peak in  
414 the 2D NMR spectra (Damodaran et al., 2002). A minor  $^{4}\text{Al}$  signal (~2%) is detected at a  
415 temperature as low as ~50 °C. The  $^{4}\text{Al}$  fraction gradually increases from ~2% at 50 °C to

Kim and Lee

416 ~4% at 200 °C, and then increases rapidly to ~7% and ~16% at 250 °C and 300 °C,  
417 respectively. The  $^{27}\text{Al}$  fraction also increases from < 1% at 50 °C to ~2.3% at 300 °C.

418 **Phase transformation from bayerite precursor.** Figure 10A shows the simulation results  
419 of the  $^{27}\text{Al}$  MAS NMR spectra of bayerite heat-treated from 25 °C to 300 °C. Although the  
420 two crystallographically inequivalent  $^{63}\text{Al}$  sites in bayerite are not fully resolved in the  
421 1D NMR spectra, the NMR parameters reported in earlier  $^{27}\text{Al}$  NMR studies were used to  
422 deconvolute NMR spectra (Bastow et al., 1994; Damodaran et al., 2002): for example, as  
423 for bayerite, the  $\delta_{\text{iso}}$ ,  $C_q$ , and  $\eta$  values of  $^{63}\text{Al}$ -1 are 9.8 ppm, 1.9 MHz, and 0.3,  
424 respectively, and those of  $^{63}\text{Al}$ -2 are 12.9 ppm, 1.7 MHz, and 0.8, respectively (Table 4).  
425 As mentioned above (Figure 4), the bayerite transforms into boehmite +  $\gamma$ -/ $\eta$ - $\text{Al}_2\text{O}_3$ . Thus,  
426 the spectra were simulated above 200 °C using the multiple  $^{41}\text{Al}$  and  $^{63}\text{Al}$  components  
427 corresponding to boehmite and  $\gamma$ -/ $\eta$ - $\text{Al}_2\text{O}_3$ .

428 The simulation results show that there are ~14% of boehmite, ~39% of  $\gamma$ -/ $\eta$ - $\text{Al}_2\text{O}_3$ ,  
429 and ~47% of bayerite at 200 °C. The  $^{41}\text{Al}$  fraction rapidly increases to ~25% as the  
430 temperature increases up to 250 °C, and then gradually up to ~27% at 300 °C, confirming  
431 that the  $\gamma$ -/ $\eta$ - $\text{Al}_2\text{O}_3$  (~91%) is predominant at 300 °C. This drastic increase  $^{41}\text{Al}$  fraction  
432 indicates that the phase transformation occurs dramatically within narrow temperature  
433 range between 200 °C and 250 °C.

434 **Phase transformation from gibbsite precursor.** Figure 10B presents the simulation  
435 results for  $^{27}\text{Al}$  MAS NMR spectra of gibbsite with varying annealing temperatures. The  
436 NMR spectra of gibbsite at 25 °C, showing the coexistence of two different  $^{63}\text{Al}$  sites, were  
437 simulated with the two components. The  $^{27}\text{Al}$  NMR parameters are  $\delta_{\text{iso}} = 12.4$  ppm,  $C_q =$   
438 4.5 MHz, and  $\eta = 0.4$  for the  $^{63}\text{Al}$ -1 site and  $\delta_{\text{iso}} = 11.3$  ppm,  $C_q = 2.3$  MHz, and  $\eta = 0.8$  for  
439 the  $^{63}\text{Al}$ -2 site (Table 5). These values are consistent with those obtained in the previous  
440  $^{27}\text{Al}$  MAS NMR study (Vyalikh et al., 2010). As the temperature increases above 200 °C,  
441 the peak shape of  $^{63}\text{Al}$  changes gradually because the gibbsite is transformed into  
442 boehmite. Note that the changes in  $^{63}\text{Al}$  peak at 200 °C is not due to the formation of  
443 metastable alumina, because the presence of  $^{41}\text{Al}$  is not observed at 200 °C. Thus, the  
444 spectrum at 200 °C was simulated using a single  $^{63}\text{Al}$  peak for boehmite and two  $^{63}\text{Al}$   
445 peaks for gibbsite. At 200 °C, the proportions of gibbsite and boehmite are ~88% and

Kim and Lee

446 ~12%, respectively. Above 250 °C, the <sup>[4]</sup>Al fraction of  $\gamma$ -/ $\eta$ -Al<sub>2</sub>O<sub>3</sub> increases from ~2% at  
447 250 °C to ~15% at 300 °C, suggesting that the phase transformation into  $\gamma$ -/ $\eta$ -Al<sub>2</sub>O<sub>3</sub> occurs  
448 at ~250 °C.

449

### 450 **Temperature-induced changes in the population of Al-(oxy)hydroxides and metastable** 451 **aluminas**

452 Figure 11 shows the variations in the <sup>[4,5]</sup>Al fractions in aluminum (oxy)hydroxides  
453 and metastable alumina with varying temperatures. At 25 °C, boehmite has ~1% of <sup>[4]</sup>Al,  
454 and the bayerite and gibbsite do not have detectable <sup>[4]</sup>Al and <sup>[5]</sup>Al. The temperature at  
455 which the increase in <sup>[4,5]</sup>Al is first observed in the NMR spectra (i.e., the onset temperature  
456 of the phase transformation into metastable alumina) depends on the type of precursor  
457 hydroxide minerals. The presence of <sup>[4,5]</sup>Al peaks is observed in boehmite even at 50 °C  
458 (~2.7%), and the <sup>[4,5]</sup>Al fraction steadily increases up to 300 °C (~18%). In contrast, in the  
459 case of bayerite and gibbsite, the <sup>[4]</sup>Al peak intensity increases abruptly from 200 °C (~11%)  
460 to 250 °C (~26%), and then increases gradually from 250 °C to 300 °C (~27%). As for gibbsite,  
461 while the <sup>[4]</sup>Al fraction is not observed in the spectra up to 200 °C, the <sup>[4]</sup>Al fraction of ~2% is  
462 observed in the spectra for 250 °C sample, and the <sup>[4]</sup>Al fraction increases rapidly to ~15% as  
463 the temperature increases to 300 °C.

464 Taking the temperature-induced changes in <sup>[4]</sup>Al fraction into consideration, Figure  
465 12 exhibits the transformation paths from boehmite (A), bayerite (B), and gibbsite (C) to  $\gamma$ -  
466 / $\eta$ -Al<sub>2</sub>O<sub>3</sub>. As shown in Figure 12A, the fraction of  $\gamma$ -/ $\eta$ -Al<sub>2</sub>O<sub>3</sub> increases continuously from  
467 ~8% at 50 °C to ~55% at 300 °C, suggesting that the phase transformation of boehmite →  $\gamma$ -  
468 / $\eta$ -Al<sub>2</sub>O<sub>3</sub> occurs at a temperature as low as ~50 °C. The threshold temperature (~50 °C) is  
469 much lower than that previously reported. These results suggest that the phase  
470 transformation from boehmite to  $\gamma$ -/ $\eta$ -Al<sub>2</sub>O<sub>3</sub> occurs in a wide temperature range than  
471 previously reported. In contrast, as shown in Figure 12B, the population of bayerite  
472 abruptly decreases from 100% (at 150 °C), through ~47% (at 200 °C), to 0% (at 250 °C),  
473 indicating that the phase transition from bayerite to boehmite +  $\gamma$ -/ $\eta$ -Al<sub>2</sub>O<sub>3</sub> occurs within a  
474 narrow temperature range. Figure 12C shows the variations in the population among  
475 gibbsite, boehmite, and  $\gamma$ -/ $\eta$ -Al<sub>2</sub>O<sub>3</sub> with varying annealing temperatures. At 200 °C, the



Kim and Lee

476 ~12% of boehmite. Above 250 °C, the fractions of both boehmite and  $\gamma$ -/ $\eta$ -Al<sub>2</sub>O<sub>3</sub> increase. In  
477 particular, the population of boehmite increases abruptly from ~12% to ~45% as the  
478 temperature increases from 200 °C to 250 °C, and then increases gradually from ~45% at 250  
479 °C to ~48% at 300 °C. The formation of  $\gamma$ -/ $\eta$ -Al<sub>2</sub>O<sub>3</sub> (~9%) is observed at 250 °C, and the  
480 fraction of  $\gamma$ -/ $\eta$ -Al<sub>2</sub>O<sub>3</sub> increases dramatically from ~9% at 250 °C to ~52% at 300 °C. At 300  
481 °C, the gibbsite is not observed. These results show that the threshold temperatures for  
482 gibbsite (~200 °C) are higher than that from boehmite (~50 °C).  
483 Although the further kinetic studies are certainly necessary (see below), the current NMR  
484 results confirm that the onset temperature and paths of transformation from aluminum  
485 (oxy)hydroxides to metastable alumina depend on the type of precursor minerals. In  
486 particular, the phase transformation of boehmite →  $\gamma$ -/ $\eta$ -Al<sub>2</sub>O<sub>3</sub> occurs at much lower  
487 temperatures (~50 °C) than those of bayerite → boehmite +  $\gamma$ -/ $\eta$ -Al<sub>2</sub>O<sub>3</sub> and gibbsite →  
488 boehmite +  $\gamma$ -/ $\eta$ -Al<sub>2</sub>O<sub>3</sub> (~200 °C). The phase transformation associated with boehmite  
489 occurs gradually within a broad temperature range. Furthermore, the NMR results show  
490 that the presence of <sup>51</sup>Al is accompanied by the phase transformation of boehmite →  $\gamma$ -/ $\eta$ -  
491 Al<sub>2</sub>O<sub>3</sub>, whereas the presence of <sup>51</sup>Al is not evident in the gibbsite-derived  $\gamma$ -/ $\eta$ -Al<sub>2</sub>O<sub>3</sub>. Note  
492 that several previous studies have suggested that the <sup>51</sup>Al is located on the surface of  $\gamma$ -/ $\eta$ -  
493 Al<sub>2</sub>O<sub>3</sub> (e.g., Kwak et al., 2009; Lee et al., 2014 and references therein). Alternatively, the  
494 earlier NMR studies of amorphous Al<sub>2</sub>O<sub>3</sub>-thin film indicated that the fractions of <sup>51</sup>Al  
495 decrease with thickness (Lee et al., 2009b; Lee et al., 2010; Lee and Ahn, 2014). Based on  
496 these results, the fraction of <sup>51</sup>Al in disordered/amorphous oxides is a proxy to the extent of  
497 structural disorder for bulk materials (Lee and Ahn, 2014; Lee et al., 2016; Lee and Ryu,  
498 2018). The current results confirm that the extent of disorder of the boehmite-derived  $\gamma$ -/ $\eta$ -  
499 Al<sub>2</sub>O<sub>3</sub> is higher than that of the gibbsite-derived  $\gamma$ -/ $\eta$ -Al<sub>2</sub>O<sub>3</sub>.

500 Therefore, the pronounced gradual phase transformation from boehmite to  $\gamma$ -/ $\eta$ -  
501 Al<sub>2</sub>O<sub>3</sub>, which occurs from ~50 °C, results from the moderate degree of structural disorder in  
502 boehmite, as also indicated from the wider X-ray diffraction peak. The difference in the  
503 extent of disorder in  $\gamma$ -/ $\eta$ -Al<sub>2</sub>O<sub>3</sub> associated with the types of precursor minerals result in the  
504 difference in the stability of metastable alumina.

Kim and Lee

505 Note that it is difficult to determine the phase transition temperature under 300 °C,  
506 because the phase transformation in the low-temperature range can be kinetically  
507 broadened (e.g., Lee et al., 2020). Thus, further extensive study for kinetic nature of  
508 dehydration is necessary. While the previous studies have shown that the heating for more  
509 than ~2 h above 300 °C does not cause significant changes in the degree of phase  
510 transformation and/or dehydration (e.g., Xu and Smith, 2012; Kim and Lee, 2013a, b; Lee  
511 and Ryu, 2018 and references therein), the effect of annealing time on the dehydration in the  
512 low-temperature range remains to be explored. Furthermore, the stability fields of  
513 metastable aluminas are dependent on their physical properties (i.e., particle sizes,  
514 permeability, and surface area) (Sun et al., 2008; Kim and Lee, 2013b; Karouia et al., 2016).  
515 Thus, the additional kinetic study of transformation with varying properties of aluminum  
516 (oxy)hydroxides remains to be considered. Nevertheless, the current results clearly  
517 demonstrate that the transformation path to metastable alumina depends on the type of  
518 precursor minerals.

### 520 Implications

521 The current <sup>27</sup>Al NMR results provide detailed information on the dehydration paths  
522 from three different aluminum (oxy)hydroxides (i.e., boehmite, bayerite, and gibbsite) to  
523 metastable alumina in the low-temperature range ( $\leq 300$  °C). By quantifying the populations  
524 of involving phases, the control of precursor minerals on the transformation paths have  
525 been systematically explored. The results demonstrate that the temperature ranges of phase  
526 transformation and the transformation paths (gradual *vs.* dramatic) depend on the extent of  
527 disorder of precursor minerals.

528 The precursor-dependent structural evolution in the low-temperature range would  
529 help to understand the geological processes involving metastable phases and their  
530 dehydration on the Earth's surface environments as the phase transformation involving  
531 metastable phases, such as  $\gamma$ -Al<sub>2</sub>O<sub>3</sub>, are common in the Earth's surface environments. For  
532 example, the recent rotary shear experiment of quartzite showed that the friction-induced  
533 melting at fault planes is partly controlled by the formation of metastable phase (such as  
534 metastable  $\beta$ -quartz), contributing to an overall fault-weakening (Lee et al., 2017). The

Kim and Lee

535 melting temperature (i.e., threshold temperature) of metastable phase is much lower than  
536 the equilibrium transition temperature (Lee et al., 2017).

537 Furthermore, the reactivity of metastable oxides in contact with an aqueous solution  
538 depends on the short-range structures (e.g., electronic environment and network topology)  
539 (e.g., Phillips et al., 2000a; Phillips et al., 2000b; Lee and Stebbins, 2003; Lee and Weiss, 2008;  
540 Li et al., 2010). The previous studies have shown that the  $^{51}\text{Al}$  sites are known to control the  
541 overall catalytic ability of metastable alumina (e.g., Kwak et al., 2007; Kwak et al., 2009; Lee  
542 et al., 2010). Because the formation of metastable  $\text{Al}_2\text{O}_3$  with  $^{51}\text{Al}$  may be prevalent at low  
543 temperature condition ( $\sim 50^\circ\text{C}$ ) as shown in the current study, the absorption of metal  
544 elements including rare-earth elements (REEs) on bauxite can be controlled by the presence  
545 of metastable alumina. It has been reported that the REEs are more enriched in boehmite-  
546 rich bauxite than in gibbsite-rich bauxite (e.g., Boni et al., 2013; Hanilçi, 2013; Radusinović et  
547 al., 2017). While speculative, this difference in REE contents may stem from the presence of  
548  $^{51}\text{Al}$  (and thus its high catalytic activity) in the boehmite-derived metastable alumina at low  
549 temperature.

550

551

### Acknowledgements

552 This study was supported by the National Research Foundation of Korea (NRF)  
553 grant funded by the Ministry of Science and ICT to Prof. Sung Keun Lee  
554 (2017R1A2A1A17069511). We deeply appreciate constructive and careful suggestions by Dr.  
555 Montouillout and an anonymous reviewer, which greatly improved the quality and clarity  
556 of the manuscript. We also thank the Associate Editor Dr. Neuville and Editor Dr. Xu.

Kim and Lee

## References cited

557

- 558 Alphonse, P., and Courty, M. (2005) Structure and thermal behavior of nanocrystalline boehmite.  
559 *Thermochimica Acta*, 425(1-2), 75-89.
- 560 Balan, E., Blanchard, M., Hochepped, J.F., and Lazzeri, M. (2008) Surface modes in the infrared  
561 spectrum of hydrous minerals: the OH stretching modes of bayerite. *Physics and Chemistry of*  
562 *Minerals*, 35(5), 279-285.
- 563 Balan, E., Lazzeri, M., Morin, G., and Mauri, F. (2006) First-principles study of the OH-stretching  
564 modes of gibbsite. *American Mineralogist*, 91(1), 115-119.
- 565 Baltisberger, J.H., Xu, Z., Stebbins, J.F., Wang, S.H., and Pines, A. (1996) Triple-quantum two-  
566 dimensional  $^{27}\text{Al}$  magic-angle spinning nuclear magnetic resonance spectroscopic study of  
567 aluminosilicate and aluminate crystals and glasses. *Journal of the American Chemical Society*,  
568 118(30), 7209-7214.
- 569 Bastow, T.J., Hall, J.S., Smith, M.E., and Steuernagel, S. (1994) Characterization of hydrated aluminas  
570 by MAS and DOR  $^{27}\text{Al}$  NMR. *Materials Letters*, 18(4), 197-200.
- 571 Boissiere, C., Nicole, L., Gervais, C., Babonneau, F., Antonietti, M., Amenitsch, H., Sanchez, C., and  
572 Grosso, D. (2006) Nanocrystalline mesoporous gamma-alumina powders "UPMC1 material"  
573 gathers thermal and chemical stability with high surface area. *Chemistry of Materials*, 18(22),  
574 5238-5243.
- 575 Bokhimi, X., Morales, A., and Valente, J.S. (2007) Sulfate ions and boehmite crystallization in a sol  
576 made with aluminum tri-sec-butoxide and 2-propanol. *Journal of Physical Chemistry C*, 111(1),  
577 103-107.
- 578 Boni, M., Rollinson, G., Mondillo, N., Balassone, G., and Santoro, L. (2013) Quantitative  
579 mineralogical characterization of karst bauxite deposits in the southern apennines, Italy.  
580 *Economic Geology*, 108(4), 813-833.
- 581 Boumaza, A., Favaro, L., Lédion, J., Sattonnay, G., Brubach, J.B., Berthet, P., Huntz, A.M., Roy, P.,  
582 and Tétot, R. (2009) Transition alumina phases induced by heat treatment of boehmite: An X-  
583 ray diffraction and infrared spectroscopy study. *Journal of Solid State Chemistry*, 182(5), 1171-  
584 1176.
- 585 Brindley, G.W., and Choe, J.O. (1961) The reaction series, gibbsite  $\rightarrow$  chi-alumina  $\rightarrow$  kappa-alumina  
586  $\rightarrow$  corundum. *American Mineralogist*, 46(7-8), 771-785.
- 587 Cai, S.-H., Rashkeev, S., Pantelides, S., and Sohlberg, K. (2002) Atomic scale mechanism of the  
588 transformation of  $\gamma$ -alumina to  $\theta$ -alumina. *Physical Review Letters*, 89(23).
- 589 Cai, S.-H., Rashkeev, S., Pantelides, S., and Sohlberg, K. (2003) Phase transformation mechanism  
590 between  $\gamma$ - and  $\theta$ -alumina. *Physical Review B*, 67(22), 224104.
- 591 Chagas, L.H., De Carvalho, G.S.G., Gil, R., Chiaro, S.S.X., Leitao, A.A., and Diniz, R. (2014)  
592 Obtaining aluminas from the thermal decomposition of their different precursors: An Al-27  
593 MAS NMR and X-ray powder diffraction studies. *Materials Research Bulletin*, 49, 216-222.
- 594 Chandran, C.V., Kirschhock, C.E.A., Radhakrishnan, S., Taulelle, F., Martens, J.A., and Breynaert, E.  
595 (2019) Alumina: discriminative analysis using 3D correlation of solid-state NMR parameters.  
596 *Chemical Society Reviews*, 48(1), 134-156.

Kim and Lee

- 597 Che, M., and Bennett, C.O. (1989) The influence of particle-size on the catalytic properties of  
598 supported metals. *Advances in Catalysis*, 36, 55-172.
- 599 Chen, B., Xu, X.S., Chen, X.M., Kong, L.J., and Chen, D.Y. (2018) Transformation behavior of gibbsite  
600 to boehmite by steam-assisted synthesis. *Journal of Solid State Chemistry*, 265, 237-243.
- 601 Chen, F.R., Davis, J.G., and Fripiat, J.J. (1992) Aluminum coordination and lewis acidity in transition  
602 aluminas. *Journal of Catalysis*, 133(2), 263-278.
- 603 Cui, J.L., Kast, M.G., Hammann, B.A., Afriyie, Y., Woods, K.N., Plassmeyer, P.N., Perkins, C.K., Ma,  
604 Z.L., Keszler, D.A., Page, C.J., Boettcher, S.W., and Hayes, S.E. (2018) Aluminum oxide thin  
605 films from aqueous solutions: Insights from solid-state NMR and dielectric response. *Chemistry  
606 of Materials*, 30(21), 7456-7463.
- 607 Damodaran, K., Rajamohanan, P.R., Chakrabarty, D., Racherla, U.S., Manohar, V., Fernandez, C.,  
608 Amoureux, J.P., and Ganapathy, S. (2002) Triple-quantum magic angle spinning Al-27 NMR of  
609 aluminum hydroxides. *Journal of the American Chemical Society*, 124(13), 3200-3201.
- 610 Digne, M., Sautet, P., Raybaud, P., Toulhoat, H., and Artacho, E. (2002) Structure and stability of  
611 aluminum hydroxides: A theoretical study. *Journal of Physical Chemistry B*, 106(20), 5155-5162.
- 612 Hanilçi, N. (2013) Geological and geochemical evolution of the Bolkardaği bauxite deposits,  
613 Karaman, Turkey: Transformation from shale to bauxite. *Journal of Geochemical Exploration*,  
614 133, 118-137.
- 615 He, J., Avnir, D., and Zhang, L. (2019) Sol-gel derived alumina glass: Mechanistic study of its  
616 structural evolution. *Acta Materialia*, 174, 418-426.
- 617 Hill, M.R., Bastow, T.J., Celotto, S., and Hill, A.J. (2007) Integrated study of the calcination cycle  
618 from gibbsite to corundum. *Chemistry of Materials*, 19(11), 2877-2883.
- 619 Hill, R.J. (1981) Hydrogen-atoms in boehmite - A single-crystal x-ray-diffraction and molecular-  
620 orbital study. *Clays and Clay Minerals*, 29(6), 435-445.
- 621 Hwang, S.-L., Shen, P., Chu, H.-T., and Yui, T.-F. (2006) A new occurrence and new data on  
622 akdalaite, a retrograde mineral from uhp whiteschist, Kokchetav massif, Northern Kazakhstan.  
623 *International Geology Review*, 48(8), 754-764.
- 624 IngramJones, V.J., Slade, R.C.T., Davies, T.W., Southern, J.C., and Salvador, S. (1996)  
625 Dehydroxylation sequences of gibbsite and boehmite: Study of differences between soak and  
626 flash calcination and of particle-size effects. *Journal of Materials Chemistry*, 6(1), 73-79.
- 627 Isobe, T., Watanabe, T., d'Espinose de la Caillerie, J.B., Legrand, A.P., and Massiot, D. (2003) Solid-  
628 state <sup>1</sup>H and <sup>27</sup>Al NMR studies of amorphous aluminum hydroxides. *Journal of Colloid and  
629 Interface Science*, 261(2), 320-324.
- 630 John, C.S., Alma, N.C.M., and Hays, G.R. (1983) Characterization of transitional alumina by solid-  
631 state magic angle spinning aluminum NMR. *Applied Catalysis*, 6(3), 341-346.
- 632 Jones, A.M., Collins, R.N., and Waite, T.D. (2011) Mineral species control of aluminum solubility in  
633 sulfate-rich acidic waters. *Geochimica et Cosmochimica Acta*, 75(4), 965-977.
- 634 Karouia, F., Boualleg, M., Digne, M., and Alphonse, P. (2016) The impact of nanocrystallite size and  
635 shape on phase transformation: Application to the boehmite/alumina transformation.  
636 *Advanced Powder Technology*, 27(4), 1814-1820.

Kim and Lee

- 637 Kim, H.N., and Lee, S.K. (2013a) Atomic structure and dehydration mechanism of amorphous silica:  
638 Insights from Si-29 and H-1 solid-state MAS NMR study of SiO<sub>2</sub> nanoparticles. *Geochimica Et*  
639 *Cosmochimica Acta*, 120, 39-64.
- 640 Kim, H.N., and Lee, S.K. (2013b) Effect of particle size on phase transitions in metastable alumina  
641 nanoparticles: A view from high-resolution solid-state Al-27 NMR study. *American*  
642 *Mineralogist*, 98(7), 1198-1210.
- 643 Kim, H.N., and Lee, S.K. (2014) Temperature-induced amorphization of Na-zeolite A: A view from  
644 multi-nuclear high-resolution solid-state NMR. *American Mineralogist*, 99(10), 1996-2007.
- 645 Kim, Y. (2015) Mineral phases and mobility of trace metals in white aluminum precipitates found in  
646 acid mine drainage. *Chemosphere*, 119, 803-811.
- 647 Kim, Y., Kim, C., Kim, P., and Yi, J. (2005) Effect of preparation conditions on the phase  
648 transformation of mesoporous alumina. *Journal of Non-Crystalline Solids*, 351(6), 550-556.
- 649 Klopogge, J.T., Duong, L.V., Wood, B.J., and Frost, R.L. (2006) XPS study of the major minerals in  
650 bauxite: Gibbsite, bayerite and (pseudo-)boehmite. *Journal of Colloid and Interface Science*,  
651 296(2), 572-576.
- 652 Klopogge, J.T., Ruan, H.D., and Frost, R.L. (2002) Thermal decomposition of bauxite minerals:  
653 infrared emission spectroscopy of gibbsite, boehmite and diaspore. *Journal of Materials Science*,  
654 37(6), 1121-1129.
- 655 Kohn, S.C., Smith, M.E., Dirken, P.J., van Eck, E.R.H., Kentgens, A.P.M., and Dupree, R. (1998)  
656 Sodium environments in dry and hydrous albite glasses: Improved Na-23 solid state NMR data  
657 and their implications for water dissolution mechanisms. *Geochimica Et Cosmochimica Acta*,  
658 62(1), 79-87.
- 659 Kraus, H., Prins, R., and Kentgens, A.P.M. (1996) A Al-27 MQMAS and off-resonance nutation NMR  
660 investigation of Mo-P/ $\gamma$ -Al<sub>2</sub>O<sub>3</sub> hydrotreating catalyst precursors. *Journal of Physical*  
661 *Chemistry*, 100(40), 16336-16345.
- 662 Krokidis, X., Raybaud, P., Gobichon, A.E., Rebours, B., Euzen, P., and Toulhoat, H. (2001)  
663 Theoretical study of the dehydration process of boehmite to gamma-alumina. *Journal of*  
664 *Physical Chemistry B*, 105(22), 5121-5130.
- 665 Kwak, J.H., Hu, J., Mei, D., Yi, C.-W., Kim, D.H., Peden, C.H.F., Allard, L.F., and Szanyi, J. (2009)  
666 Coordinatively unsaturated Al<sup>3+</sup> centers as binding sites for active catalyst phases of platinum  
667 on  $\gamma$ -Al<sub>2</sub>O<sub>3</sub>. *Science*, 325(5948), 1670.
- 668 Kwak, J.H., Hu, J.Z., Kim, D.H., Szanyi, J., and Peden, C.H.F. (2007) Penta-coordinated Al<sup>3+</sup> ions as  
669 preferential nucleation sites for BaO on  $\gamma$ -Al<sub>2</sub>O<sub>3</sub>: An ultra-high-magnetic field <sup>27</sup>Al MAS NMR  
670 study. *Journal of Catalysis*, 251(1), 189-194.
- 671 Kwak, J.H., Hu, J.Z., Lukaski, A., Kim, D.H., Szanyi, J., and Peden, C.H.F. (2008) Role of  
672 pentacoordinated Al<sup>3+</sup> ions in the high temperature phase transformation of gamma-Al<sub>2</sub>O<sub>3</sub>.  
673 *Journal of Physical Chemistry C*, 112(25), 9486-9492.
- 674 Le Caer, G., and Brand, R.A. (1998) General models for the distributions of electric field gradients in  
675 disordered solids. *Journal of Physics-Condensed Matter*, 10(47), 10715-10774.

Kim and Lee

- 676 Lee, D., Duong, N.T., Lafon, O., and De Paëpe, G. (2014) Primostrato solid-state NMR enhanced by  
677 dynamic nuclear polarization: Pentacoordinated Al<sup>3+</sup> Ions are only located at the surface of  
678 hydrated  $\gamma$ -alumina. *The Journal of Physical Chemistry C*, 118(43), 25065-25076.
- 679 Lee, J., Jeon, H., Oh, D.G., Szanyi, J., and Kwak, J.H. (2015) Morphology-dependent phase  
680 transformation of  $\gamma$ -Al<sub>2</sub>O<sub>3</sub>. *Applied Catalysis A: General*, 500, 58-68.
- 681 Lee, S.K. (2011) Simplicity in melt densification in multicomponent magmatic reservoirs in Earth's  
682 interior revealed by multinuclear magnetic resonance. *Proceedings of the National Academy of*  
683 *Sciences of the United States of America*, 108(17), 6847-6852.
- 684 Lee, S.K., and Ahn, C.W. (2014) Probing of 2 dimensional confinement-induced structural transitions  
685 in amorphous oxide thin film. *Scientific Reports*, 4(1), 4200.
- 686 Lee, S.K., Deschamps, M., Hiet, J., Massiot, D., and Park, S.Y. (2009a) Connectivity and proximity  
687 between quadrupolar nuclides in oxide glasses: insights from through-bond and through-space  
688 correlations in solid-state NMR. *Journal of Physical Chemistry B*, 113(15), 5162-7.
- 689 Lee, S.K., Han, R., Kim, E.J., Jeong, G.Y., Khim, H., and Hirose, T. (2017) Quasi-equilibrium melting  
690 of quartzite upon extreme friction. *Nature Geoscience*, 10(6), 436-441.
- 691 Lee, S.K., Kim, H.-I., Kim, E.J., Mun, K.Y., and Ryu, S. (2016) Extent of disorder in magnesium  
692 aluminosilicate glasses: Insights from <sup>27</sup>Al and <sup>17</sup>O NMR. *Journal of Physical Chemistry C*,  
693 120(1), 737-749.
- 694 Lee, S.K., Lee, S.B., Park, S.Y., Yi, Y.S., and Ahn, C.W. (2009b) Structure of amorphous aluminum  
695 oxide. *Physical Review Letters*, 103(9).
- 696 Lee, S.K., Mun, K.Y., Kim, Y.-H., Lhee, J., Okuchi, T., and Lin, J.-F. (2020) Degree of Permanent  
697 Densification in Oxide Glasses upon Extreme Compression up to 24 GPa at Room Temperature.  
698 *The Journal of Physical Chemistry Letters*, 11(8), 2917-2924.
- 699 Lee, S.K., Park, S.Y., Yi, Y.S., and Moon, J. (2010) Structure and disorder in amorphous alumina thin  
700 films: Insights from high-resolution solid-state NMR. *Journal of Physical Chemistry C*, 114(32),  
701 13890-13894.
- 702 Lee, S.K., and Ryu, S. (2018) Probing of triply coordinated oxygen in amorphous Al<sub>2</sub>O<sub>3</sub>. *Journal of*  
703 *Physical Chemistry Letters*, 9(1), 150-156.
- 704 Lee, S.K., and Stebbins, J.F. (2003) O atom sites in natural kaolinite and muscovite: O-17 MAS and  
705 3QMAS NMR study. *American Mineralogist*, 88(4), 493-500.
- 706 Lee, S.K., and Weiss, C.A. (2008) Multiple oxygen sites in synthetic phyllosilicates with expandable  
707 layers: <sup>17</sup>O solid-state NMR study. *American Mineralogist*, 93(7), 1066-1071.
- 708 Lee, S.R., Han, Y.S., Park, M., Park, G.S., and Choy, J.H. (2003) Nanocrystalline sodalite from Al<sub>2</sub>O<sub>3</sub>  
709 pillared clay by solid-solid transformation. *Chemistry of Materials*, 15(25), 4841-4845.
- 710 Levin, I., and Brandon, D. (1998) Metastable alumina polymorphs: Crystal structures and transition  
711 sequences. *Journal of the American Ceramic Society*, 81(8), 1995-2012.
- 712 Li, W., Feng, J., Kwon, K.D., Kubicki, J.D., and Phillips, B.L. (2010) Surface speciation of phosphate  
713 on boehmite ( $\gamma$ -AlOOH) determined from NMR spectroscopy. *Langmuir*, 26(7), 4753-4761.
- 714 Lippens, B.C., and De Boer, J.H. (1964) Study of phase transformations during calcination of  
715 aluminum hydroxides by selected area electron diffraction. *Acta Crystallographica*, 17(10),  
716 1312-1321.

Kim and Lee

- 717 Lippmaa, E., Samoson, A., and Magi, M. (1986) High-resolution  $^{27}\text{Al}$  NMR of aluminosilicates.  
718 *Journal of the American Chemical Society*, 108(8), 1730-1735.
- 719 MacKenzie, K.J.D., Temuujin, J., Smith, M.E., Angerer, P., and Kameshima, Y. (2000) Effect of  
720 mechanochemical activation on the thermal reactions of boehmite ( $\gamma\text{-AlOOH}$ ) and  $\gamma\text{-Al}_2\text{O}_3$ .  
721 *Thermochimica Acta*, 359(1), 87-94.
- 722 Maruthiprasad, B.S., Sastri, M.N., Rajagopal, S., Seshan, K., Krishnamurthy, K.R., and Rao, T.S.R.P.  
723 (1988) Thermal analysis of alumina precursors prepared by 'PFHS' methods. *Journal of thermal*  
724 *analysis*, 34(4), 1023-1030.
- 725 Massiot, D., Fayon, F., Capron, M., King, I., Le Calve, S., Alonso, B., Durand, J.O., Bujoli, B., Gan,  
726 Z.H., and Hoatson, G. (2002) Modelling one- and two-dimensional solid-state NMR spectra.  
727 *Magnetic Resonance in Chemistry*, 40(1), 70-76.
- 728 Mercury, J.M.R., Pena, P., de Aza, A.H., Sheptyakov, D., and Turrillas, X. (2006) On the  
729 decomposition of synthetic gibbsite studied by neutron thermodiffraction. *Journal of the*  
730 *American Ceramic Society*, 89(12), 3728-3733.
- 731 Neuville, D.R., Cormier, L., and Massiot, D. (2004) Al environment in tectosilicate and peraluminous  
732 glasses: A Al-27 MQ-MAS NMR, Raman, and XANES investigation. *Geochimica Et*  
733 *Cosmochimica Acta*, 68(24), 5071-5079.
- 734 O'Dell, L.A., Savin, S.L., Chadwick, A.V., and Smith, M.E. (2007) A  $^{27}\text{Al}$  MAS NMR study of a sol-gel  
735 produced alumina: Identification of the NMR parameters of the theta- $\text{Al}_2\text{O}_3$  transition alumina  
736 phase. *Solid State Nucl Magn Reson*, 31(4), 169-73.
- 737 Paglia, G., Bozin, E.S., and Billinge, S.J.L. (2006) Fine-scale nanostructure in gamma- $\text{Al}_2\text{O}_3$ .  
738 *Chemistry of Materials*, 18(14), 3242-3248.
- 739 Paglia, G., Buckley, C., Rohl, A., Hunter, B., Hart, R., Hanna, J., and Byrne, L. (2003) Tetragonal  
740 structure model for boehmite-derived  $\gamma$ -alumina. *Physical Review B*, 68(14).
- 741 Park, S.Y., and Lee, S.K. (2019) Effect of composition on isotropic chemical shift of Na silicate and  
742 aluminosilicate glasses using solid state NMR. *Journal of the Mineralogical Society of Korea*,  
743 32(1), 41-49.
- 744 Pecharroman, C., Sobrados, I., Iglesias, J.E., Gonzalez-Carreno, T., and Sanz, J. (1999) Thermal  
745 evolution of transitional aluminas followed by NMR and IR spectroscopies. *Journal of Physical*  
746 *Chemistry B*, 103(30), 6160-6170.
- 747 Perander, L.M., Zujovic, Z.D., Groutso, T., Hyland, M.M., Smith, M.E., O'Dell, L.A., and Metson, J.B.  
748 (2007) Characterization of metallurgical-grade aluminas and their precursors by  $^{27}\text{Al}$  NMR and  
749 XRD. *Canadian Journal of Chemistry-Revue Canadienne De Chimie*, 85(10), 889-897.
- 750 Phillips, B.L., Casey, W.H., and Karlsson, M. (2000a) Bonding and reactivity at oxide mineral  
751 surfaces from model aqueous complexes. *Nature*, 404(6776), 379-382.
- 752 Phillips, B.L., Xu, H.W., Heaney, P.J., and Navrotsky, A. (2000b) Si-29 and Al-27 MAS-NMR  
753 spectroscopy of beta-eucryptite ( $\text{LiAlSiO}_4$ ): The enthalpy of Si,Al ordering. *American*  
754 *Mineralogist*, 85(1), 181-188.
- 755 Radusinović, S., Jelenković, R., Pačevski, A., Simić, V., Božović, D., Holclajtner-Antunović, I., and  
756 Životić, D. (2017) Content and mode of occurrences of rare earth elements in the Zagrad karstic  
757 bauxite deposit (Nikšić area, Montenegro). *Ore Geology Reviews*, 80, 406-428.



Kim and Lee

- 758 Rouquerol, J., Rouquerol, F., and Ganteaume, M. (1975) Thermal-decomposition of gibbsite under  
759 low-pressures .1. Formation of boehmitic phase. *Journal of Catalysis*, 36(1), 99-110.
- 760 Sabarinathan, V., Ramasamy, S., and Ganapathy, S. (2010) Perturbations to <sup>27</sup>Al electric field  
761 gradients in nanocrystalline alpha-Al<sub>2</sub>O<sub>3</sub> studied by high-resolution solid-state NMR. *Journal of*  
762 *Physical Chemistry B*, 114(5), 1775-1781.
- 763 Serna, C.J., White, J.L., and Hem, S.L. (1977) Hydrolysis of aluminum-tri-(sec-butoxide) in ionic and  
764 nonionic media. *Clays and Clay Minerals*, 25(6), 384-391.
- 765 Shen, S.C., Chen, Q., Chow, P.S., Tan, G.H., Zeng, X.T., Wang, Z., and Tan, R.B.H. (2007) Steam-  
766 assisted solid wet-gel synthesis of high-quality nanorods of boehmite and alumina. *Journal of*  
767 *Physical Chemistry C*, 111(2), 700-707.
- 768 Sohlberg, K., Pantelides, S.T., and Pennycook, S.J. (2001) Surface reconstruction and the difference in  
769 surface acidity between gamma- and eta-alumina. *Journal of the American Chemical Society*,  
770 123(1), 26-29.
- 771 Stebbins, J.F., Kroeker, S., Lee, S.K., and Kiczenski, T.J. (2000) Quantification of five- and six-  
772 coordinated aluminum ions in aluminosilicate and fluoride-containing glasses by high-field,  
773 high-resolution Al-27 NMR. *Journal of Non-Crystalline Solids*, 275(1-2), 1-6.
- 774 Sun, Z.X., Zheng, T.T., Bo, Q.B., Du, M., and Forsling, W. (2008) Effects of calcination temperature  
775 on the pore size and wall crystalline structure of mesoporous alumina. *J Colloid Interface Sci*,  
776 319(1), 247-51.
- 777 Tilley, D.B., and Eggleton, R.A. (1996) The natural occurrence of eta-alumina ( $\eta$ -Al<sub>2</sub>O<sub>3</sub>) in bauxite.  
778 *Clays and Clay Minerals*, 44(5), 658-664.
- 779 Tsukada, T., Segawa, H., Yasumori, A., and Okada, K. (1999) Crystallinity of boehmite and its effect  
780 on the phase transition temperature of alumina. *Journal of Materials Chemistry*, 9(2), 549-553.
- 781 Vaudry, F., Khodabandeh, S., and Davis, M.E. (1996) Synthesis of pure alumina mesoporous  
782 materials. *Chemistry of Materials*, 8(7), 1451-1464.
- 783 Vyalikh, A., Zesewitz, K., and Scheler, U. (2010) Hydrogen bonds and local symmetry in the crystal  
784 structure of gibbsite. *Magnetic Resonance in Chemistry*, 48(11), 877-881.
- 785 Xu, B., and Smith, P. (2012) Dehydration kinetics of boehmite in the temperature range 723–873K.  
786 *Thermochimica Acta*, 531, 46-53.
- 787 Zhou, R.S., and Snyder, R.L. (1991) Structures and transformation mechanisms of the  $\eta$ ,  $\gamma$  and  $\theta$   
788 transition aluminas. *Acta Crystallographica Section B*, 47(5), 617-630.

Kim and Lee

### List of figure captions

789

790 **Figure 1** | Crystal structures of (A) boehmite, (B) bayerite, (C) gibbsite, and (D)  $\gamma$ - $\text{Al}_2\text{O}_3$ . See  
791 Table 1 for details of crystal structures.

792 **Figure 2** | (A) XRD patterns for boehmite with varying annealing temperatures up to 300  
793 °C. Red and blue vertical lines correspond to the peak positions and intensities of  
794 boehmite (JCPDS file no. 00-021-1307),  $\gamma$ - $\text{Al}_2\text{O}_3$  (JCPDS file no. 01-079-1558), and  $\eta$ -  
795  $\text{Al}_2\text{O}_3$  (JCPDS file no. 00-21-0010), respectively.  $^{27}\text{Al}$  MAS NMR spectra for boehmite  
796 with varying temperatures at 11.7 T (B) and 14.1 T (C).

797 **Figure 3** | The enlarged  $^{27}\text{Al}$  MAS NMR spectra for boehmite with varying annealing  
798 temperatures obtained at 11.7 T (left) and 14.1 T (right).

799 **Figure 4** | (A) XRD patterns for bayerite with varying annealing temperatures up to 300 °C.  
800 Black, red, and blue vertical lines correspond to the peak positions and intensities of  
801 bayerite (JCPDS file no. 01-083-2256), boehmite (JCPDS file no. 00-021-1307) and  $\eta$ -  
802  $\text{Al}_2\text{O}_3$  (JCPDS file no. 00-21-0010), respectively. (B)  $^{27}\text{Al}$  MAS NMR spectra at 11.7 T for  
803 bayerite with varying temperatures. (C) Comparison of  $^{27}\text{Al}$  NMR spectra for bayerite  
804 at 25 °C (black line) and 300 °C (red line). The enlarged  $^{27}\text{Al}$  NMR spectra (D) are also  
805 shown to manifest the evolution of  $^{41}\text{Al}$  sites.

806 **Figure 5** | (A) XRD patterns for gibbsite with varying annealing temperatures up to 300 °C.  
807 Black, red, and blue vertical lines correspond to the peak positions and intensities of  
808 gibbsite (JCPDS file no. 01-070-2038), boehmite (JCPDS file no. 00-021-1307), and  $\gamma$ - $\text{Al}_2\text{O}_3$   
809 (JCPDS file no. 01-079-1558), respectively. (B)  $^{27}\text{Al}$  MAS NMR spectra at 11.7 T for  
810 gibbsite with varying temperatures. (C) Comparison of  $^{27}\text{Al}$  NMR spectra for gibbsite at  
811 25 °C (black line) and 300 °C (red line). The enlarged  $^{27}\text{Al}$  NMR spectra (D) are also  
812 shown to manifest the evolution of  $^{41}\text{Al}$  sites.

813 **Figure 6** |  $^{27}\text{Al}$  3QMAS NMR spectra for boehmite with varying annealing temperature (as  
814 labeled) at 9.4 T. The contour lines are drawn from 8 to 98% relative intensity with a 6%  
815 increment. Four additional contour lines (1, 2.5, 4, and 6%) were added in  $^{4,5}\text{Al}$  sites to  
816 better show low-intensity peaks (see SI-1 for 2D spectra without noise removal)

817 **Figure 7** | (A)  $^{61}\text{Al}$  peaks in  $^{27}\text{Al}$  3QMAS NMR spectra for boehmite with varying annealing  
818 temperature up to 300 °C. Contour lines are drawn from 8 to 98% of the relative  
819 intensity with increment of 5%. (B) Expected center of gravity for boehmite and  $\gamma$ -/ $\eta$ -

Kim and Lee

820  $\text{Al}_2\text{O}_3$  calculated on the basis of the current simulation (open symbols) and previous  
821 works [solid symbols, black circle (Damodaran et al., 2002); red triangle (Kraus et al.,  
822 1996); red inverted-triangle (Pecharroman et al., 1999); red diamond (Perander et al.,  
823 2007); red circle (Kim and Lee, 2013)]. Black and red symbols refer to boehmite and  $\gamma$ -  
824  $\eta\text{-Al}_2\text{O}_3$ , respectively.

825 **Figure 8** | Simulation of  $^{27}\text{Al}$  MAS NMR spectra obtained at 11.7 T for boehmite with  
826 varying annealing temperatures up to 300 °C. Thick gray lines refer to the experimental  
827 spectra, and thin black lines refer to the simulation results. Each component used in the  
828 simulation is shown as labeled.

829 **Figure 9** | Simulation of  $^{27}\text{Al}$  MAS NMR spectra obtained at 14.1 T for boehmite with  
830 varying annealing temperatures up to 300 °C. Thick gray lines refer to the experimental  
831 spectra, and thin black lines refer to the simulation results. Each component used in the  
832 simulation is shown as labeled.

833 **Figure 10** | Simulation of  $^{27}\text{Al}$  MAS NMR spectra obtained at 11.7 T for bayerite (left) and  
834 gibbsite (right) with varying annealing temperatures up to 300 °C. Thick gray lines  
835 refer to the experimental spectra, and thin black lines refer to the simulation results.  
836 Each component used in the simulation is shown as labeled.

837 **Figure 11** | Variation in the  $^{[4,5]}\text{Al}$  fraction for boehmite (blue squares), bayerite (red circles),  
838 and gibbsite (black triangles) with varying temperatures. The smooth lines are to guide  
839 the eye only.

840 **Figure 12** | (A) Variations in the populations of (A) boehmite and  $\gamma$ -/ $\eta\text{-Al}_2\text{O}_3$ , (B) bayerite  
841 and  $\gamma$ -/ $\eta\text{-Al}_2\text{O}_3$  + boehmite, and (C) gibbsite, boehmite and  $\gamma$ -/ $\eta\text{-Al}_2\text{O}_3$  with varying  
842 annealing temperatures. The smooth lines are to guide the eye only. The shaded areas  
843 show the phase transformation temperature ranges from precursor minerals to  
844 metastable alumina.

## Tables

**Table 1 |** Crystallographic information of aluminum (oxy)hydroxide precursor minerals (i.e., boehmite, bayerite, and gibbsite) and metastable alumina (i.e.,  $\gamma$ - and  $\eta$ -Al<sub>2</sub>O<sub>3</sub>)

	<b>Boehmite</b>	<b>Bayerite</b>	<b>Gibbsite</b>
Al coordination	[ <sup>6</sup> Al]-1 100%	[ <sup>6</sup> Al]-1 50%	[ <sup>6</sup> Al]-1 50%
		[ <sup>6</sup> Al]-2 50%	[ <sup>6</sup> Al]-2 50%
Crystal system	Orthorhombic	Monoclinic	Monoclinic
Space group	Cmcm	P2 <sub>1</sub> /m	P2 <sub>1</sub> /m
Lattice parameter (Å)			
A	2.8796	5.096	8.742
B	12.205	8.729	5.112
C	3.761	9.489	9.801
Density (g/cm <sup>3</sup> )	3.04	2.42	2.38-2.42
Reference	Hill (1981)	Balan et al. (2008)	Balan et al. (2006)
	<b><math>\gamma</math>-Al<sub>2</sub>O<sub>3</sub></b>	<b><math>\eta</math>-Al<sub>2</sub>O<sub>3</sub></b>	
Crystal system	Cubic (defect spinel)	Cubic (defect spinel)	
Space group	Fd $\bar{3}$ m	Fd $\bar{3}$ m	
Lattice parameter (Å)			
A (=B=C)	7.911	7.914	
Idealized formula	[ <sup>4</sup> Al] $\square_{1/3}$ [ <sup>6</sup> Al] <sub>5/3</sub> O <sub>4</sub>	[ <sup>4</sup> Al] <sub>2/3</sub> $\square_{1/3}$ [ <sup>6</sup> Al] <sub>2</sub> O <sub>4</sub>	
[ <sup>4</sup> Al]:[ <sup>6</sup> Al]	1:3 (~25:75)	3:5 (~38:62)	
Reference	Lippen and de Bohr (1964)	Zhou and Snyder (1991)	

**Table 2** |  $^{27}\text{Al}$  NMR parameters for aluminum (oxy)hydroxides and metastable alumina

Reference	Method	Phase	Larmor frequency (MHz)	$^{n}\text{Al}$	$\delta_{\text{iso}}$ (ppm) <sup>a</sup>	$\Delta\delta_{\text{iso}}$ <sup>b</sup>	$C_q$ (MHz) <sup>c</sup>	$\eta^d$	Site fraction (%)
Damodaran et al. (2002)	MQMAS	Boehmite	130.3	$^{6}\text{Al}$	12.6	-	1.8-2.8	0.5-1.0	100
				$^{6}\text{Al}$ -1	9.1	-	$1.9 \pm 0.1$	$0.25 \pm 0.05$	50
		$^{6}\text{Al}$ -2		13.1	-	$1.4 \pm 0.1$	$0.80 \pm 0.05$	50	
		Gibbsite		$^{6}\text{Al}$ -1	11.6	-	$2.2 \pm 0.2$	$0.75 \pm 0.05$	50
				$^{6}\text{Al}$ -2	17.2	-	$4.7 \pm 0.2$	$1.00 \pm 0.05$	50
Vyalikh et al. (2010)	MAS	Gibbsite	130.3	$^{6}\text{Al}$ -1	$11.3 \pm 0.2$	-	$2.2 \pm 0.2$	$0.7 \pm 0.1$	$50 \pm 5$
				$^{6}\text{Al}$ -2	$13.6 \pm 0.2$	-	$4.6 \pm 0.2$	$0.4 \pm 0.1$	$50 \pm 5$
Ferreira et al. (2001)	Theoretical Calculation	Boehmite	-	$^{6}\text{Al}$	11.7-12.4	-	2.1-2.3	0.5-0.7	100
Kim and Lee (2013)	MAS (Czjzek)	$\gamma\text{-Al}_2\text{O}_3$	130.3	$^{6}\text{Al}$	$14.0 \pm 1.0$	$6.5 \pm 2.5$	$4.6 \pm 1.0$	-	$68 \pm 3$
				$^{4}\text{Al}$	$72.5 \pm 1.0$	$10 \pm 3$	$5.7 \pm 1.0$	-	$32 \pm 3$
de Lacaillerie et al. (2008)	MAS (Czjzek)	$\gamma\text{-Al}_2\text{O}_3$	130.3	$^{6}\text{Al}$	13.8	-	-	-	67
				$^{4}\text{Al}$	73.8	-	-	-	33
Kraus et al. (1996)	MAS	$\gamma\text{-Al}_2\text{O}_3$	130.3	$^{6}\text{Al}$	$9 \pm 1$	-	$4.5 \pm 0.5$	0.3	-
				$^{4}\text{Al}$	$67 \pm 1$	-	$5.0 \pm 0.5$	0.3	-
Pecharroman et al. (1999)	MAS	$\eta\text{-Al}_2\text{O}_3$	104.3	$^{6}\text{Al}$	$14.5 \pm 0.2$	-	$3.9 \pm 0.2$	$0.4 \pm 0.1$	69-78
				$^{4}\text{Al}$	$76.5 \pm 0.2$	-	$4.5 \pm 0.2$	$0.7 \pm 0.1$	22-31
		$\gamma\text{-Al}_2\text{O}_3$		$^{6}\text{Al}$	$15.2 \pm 0.2$	-	$3.7 \pm 0.2$	$0.4 \pm 0.1$	69-76
				$^{5}\text{Al}$	-	-	-	-	3-6.5
				$^{4}\text{Al}$	$78.5 \pm 0.2$	-	$4.7 \pm 0.2$	$0.7 \pm 0.1$	21-26

<sup>a</sup>) Isotropic chemical shift

<sup>b</sup>) Full-width at half maximum of the distribution of the isotropic chemical shift in the Czjzek model

<sup>c</sup>) Quadrupolar coupling constant

<sup>d</sup>) Asymmetry parameter

**Table 3 |**  $^{27}\text{Al}$  NMR parameters for the simulation of the NMR spectra for boehmite with varying temperature at 11.7 T and 14.1 T.

Precursor mineral	T (°C)	Phase	$^{[n]}\text{Al}$	$\delta_{\text{iso}}$ (ppm) <sup>a</sup>	$C_q$ (MHz) <sup>b</sup>	$\Delta\delta_{\text{iso}}$ <sup>c</sup>	$^{[n]}\text{Al}$ fraction for each phase (%) <sup>d,*</sup>
Boehmite	25	Boehmite	$^{[6]}\text{Al}$	$10.8 \pm 1.5$	$2.7 \pm 0.3$	$4 \pm 2$	$99 \pm 1$
			$^{[4]}\text{Al}$	$73.0 \pm 1.5$	$5.0 \pm 1.0$	$4 \pm 2$	< 1
	50	Boehmite $\gamma$ -/ $\eta$ - $\text{Al}_2\text{O}_3$	$^{[6]}\text{Al}$	$10.5 \pm 1.5$	$2.8 \pm 0.3$	$4 \pm 2$	$93 \pm 3$
			$^{[6]}\text{Al}$	$11.4 \pm 1.5$	$4.8 \pm 0.5$	$6 \pm 2$	$4 \pm 3$
			$^{[5]}\text{Al}$	$41.3 \pm 1.5$	$5.7 \pm 1.0$	$6 \pm 2$	< 1
			$^{[4]}\text{Al}$	$73.4 \pm 1.5$	$5.1 \pm 1.0$	$7 \pm 2$	$2 \pm 3$
	110	Boehmite $\gamma$ -/ $\eta$ - $\text{Al}_2\text{O}_3$	$^{[6]}\text{Al}$	$10.5 \pm 1.5$	$2.8 \pm 0.3$	$4 \pm 2$	$92 \pm 3$
			$^{[6]}\text{Al}$	$11.4 \pm 1.5$	$4.8 \pm 0.5$	$7 \pm 2$	$5 \pm 3$
			$^{[5]}\text{Al}$	$41.3 \pm 1.5$	$5.7 \pm 1.0$	$6 \pm 2$	< 1
			$^{[4]}\text{Al}$	$73.6 \pm 1.5$	$5.3 \pm 1.0$	$7 \pm 2$	$2 \pm 3$
	150	Boehmite $\gamma$ -/ $\eta$ - $\text{Al}_2\text{O}_3$	$^{[6]}\text{Al}$	$10.2 \pm 1.5$	$2.8 \pm 0.3$	$4 \pm 2$	$87 \pm 3$
			$^{[6]}\text{Al}$	$11.1 \pm 1.5$	$4.8 \pm 0.5$	$7 \pm 2$	$8 \pm 3$
			$^{[5]}\text{Al}$	$41.0 \pm 1.5$	$6.0 \pm 1.0$	$6 \pm 2$	< 2
			$^{[4]}\text{Al}$	$73.4 \pm 1.5$	$5.6 \pm 1.0$	$9 \pm 2$	$3 \pm 3$
	200	Boehmite $\gamma$ -/ $\eta$ - $\text{Al}_2\text{O}_3$	$^{[6]}\text{Al}$	$10.5 \pm 1.5$	$2.8 \pm 0.3$	$5 \pm 2$	$85 \pm 3$
			$^{[6]}\text{Al}$	$12.2 \pm 1.5$	$4.8 \pm 0.5$	$7 \pm 2$	$9 \pm 3$
			$^{[5]}\text{Al}$	$41.0 \pm 1.5$	$6.0 \pm 1.0$	$6 \pm 2$	< 2
			$^{[4]}\text{Al}$	$73.9 \pm 1.5$	$5.7 \pm 1.0$	$10 \pm 2$	$4 \pm 3$
	250	Boehmite $\gamma$ -/ $\eta$ - $\text{Al}_2\text{O}_3$	$^{[6]}\text{Al}$	$10.1 \pm 1.5$	$2.8 \pm 0.3$	$5 \pm 2$	$78 \pm 3$
			$^{[6]}\text{Al}$	$11.8 \pm 1.5$	$4.8 \pm 0.5$	$7 \pm 2$	$14 \pm 3$
			$^{[5]}\text{Al}$	$41.2 \pm 1.5$	$6.0 \pm 1.0$	$6 \pm 2$	< 2
			$^{[4]}\text{Al}$	$73.7 \pm 1.5$	$5.7 \pm 1.0$	$9 \pm 2$	$6 \pm 3$
	300	Boehmite $\gamma$ -/ $\eta$ - $\text{Al}_2\text{O}_3$	$^{[6]}\text{Al}$	$10.6 \pm 1.5$	$2.8 \pm 0.3$	$5 \pm 2$	$45 \pm 3$
			$^{[6]}\text{Al}$	$12.1 \pm 1.5$	$4.8 \pm 0.5$	$8 \pm 2$	$36 \pm 3$
			$^{[5]}\text{Al}$	$41.0 \pm 1.5$	$6.0 \pm 1.0$	$7 \pm 2$	< 3
			$^{[4]}\text{Al}$	$73.9 \pm 1.5$	$5.7 \pm 1.0$	$10 \pm 2$	$16 \pm 3$

Note: The  $^{27}\text{Al}$  NMR spectra for boehmite at 25, 50, 110, 200, and 300 °C were simulated simultaneously at 11.7 T and 14.1 T.

<sup>a</sup>) Isotropic chemical shift

<sup>b</sup>) Quadrupolar coupling constant

<sup>c</sup>) Full-width at half maximum of the distribution of the isotropic chemical shift in the Czejk model

<sup>d</sup>)  $^{[n]}\text{Al}$  fraction for each phase =  $^{[n]}\text{Al}$  for each phase/total area under NMR spectra

\*The uncertainties of each Al site fraction stem from the deviation between experimental and simulated spectra (~1.5%), the contribution from the adjusted NMR parameters (~1.5%), the contribution of spinning sidebands (~1.5%), and phasing of the NMR spectrum (~1.5%). Considering these uncertainties, the total error bar of ±3% is estimated.

Kim and Lee

**Table 4** |  $^{27}\text{Al}$  NMR parameters for the simulation of the NMR spectra for bayerite with varying temperature at 11.7 T.

Precursor mineral	Larmor frequency (MHz)	T (°C)	Phase	$^{[n]}\text{Al}$	$\delta_{\text{iso}}$ (ppm) <sup>a</sup>	$C_q$ (MHz) <sup>b</sup>	$\eta^c$	$\Delta\delta_{\text{iso}}^d$	$^{[n]}\text{Al}$ fraction for each phase (%) <sup>e,*</sup>
Bayerite	130.28	25	Bayerite	$^{[6]}\text{Al-1}$	$9.8 \pm 0.5$	$1.9 \pm 0.3$	$0.3 \pm 0.1$	-	$51 \pm 3$
				$^{[6]}\text{Al-2}$	$12.9 \pm 0.5$	$1.7 \pm 0.3$	$0.8 \pm 0.1$	-	$49 \pm 3$
		110	Bayerite	$^{[6]}\text{Al-1}$	$9.8 \pm 0.5$	$1.9 \pm 0.3$	$0.3 \pm 0.1$	-	$50 \pm 3$
				$^{[6]}\text{Al-2}$	$13.0 \pm 0.5$	$1.7 \pm 0.3$	$0.8 \pm 0.1$	-	$50 \pm 3$
		150	Bayerite	$^{[6]}\text{Al-1}$	$9.8 \pm 0.5$	$2.0 \pm 0.3$	$0.3 \pm 0.1$	-	$51 \pm 3$
				$^{[6]}\text{Al-2}$	$12.9 \pm 0.5$	$1.7 \pm 0.3$	$0.8 \pm 0.1$	-	$49 \pm 3$
		200	Bayerite	$^{[6]}\text{Al-1}$	$9.9 \pm 0.5$	$2.0 \pm 0.3$	$0.3 \pm 0.1$	-	$23 \pm 3$
				$^{[6]}\text{Al-2}$	$13.1 \pm 0.5$	$1.6 \pm 0.3$	$0.8 \pm 0.1$	-	$24 \pm 3$
			Boehmite $\gamma$ -/ $\eta$ - $\text{Al}_2\text{O}_3$	$^{[6]}\text{Al}$	$11.2 \pm 1.0$	$2.7 \pm 0.5$		$4 \pm 1$	$14 \pm 3$
				$^{[6]}\text{Al}$	$13.5 \pm 1.5$	$4.4 \pm 0.5$	-	$5 \pm 1$	$27 \pm 3$
				$^{[4]}\text{Al}$	$73.0 \pm 1.5$	$5.4 \pm 0.5$	-	$8 \pm 1$	$12 \pm 3$
		250	Boehmite $\gamma$ -/ $\eta$ - $\text{Al}_2\text{O}_3$	$^{[6]}\text{Al}$	$10.9 \pm 1.5$	$2.7 \pm 0.5$	-	$4 \pm 1$	$14 \pm 3$
				$^{[6]}\text{Al}$	$13.5 \pm 1.5$	$4.8 \pm 0.5$	-	$5 \pm 1$	$60 \pm 3$
				$^{[4]}\text{Al}$	$72.8 \pm 1.5$	$5.4 \pm 0.5$	-	$8 \pm 1$	$26 \pm 3$
		300	Boehmite $\gamma$ -/ $\eta$ - $\text{Al}_2\text{O}_3$	$^{[6]}\text{Al}$	$10.9 \pm 1.5$	$2.7 \pm 0.5$	-	$4 \pm 1$	$9 \pm 3$
				$^{[6]}\text{Al}$	$13.2 \pm 1.5$	$4.8 \pm 0.5$	-	$5 \pm 1$	$64 \pm 3$
				$^{[4]}\text{Al}$	$72.8 \pm 1.5$	$5.4 \pm 0.5$	-	$8 \pm 1$	$27 \pm 3$

<sup>a</sup>) Isotropic chemical shift

<sup>b</sup>) Quadrupolar coupling constant

<sup>c</sup>) Asymmetry parameter

<sup>d</sup>) Full-width at half maximum of the distribution of the isotropic chemical shift in the Czepek model

<sup>e</sup>)  $^{[n]}\text{Al}$  fraction for each phase =  $^{[n]}\text{Al}$  for each phase/total area under NMR spectra

\*The uncertainties of each Al site fraction stem from the deviation between experimental and simulated spectra (~1.5%), the contribution from the adjusted NMR parameters (~1.5%), the contribution of spinning sidebands (~1.5%), and phasing of the NMR spectrum (~1.5%). Considering these uncertainties, the total error bar of  $\pm 3\%$  is estimated.

Kim and Lee

**Table 5 |**  $^{27}\text{Al}$  NMR parameters for the simulation of the NMR spectra for gibbsite with varying temperature at 11.7 T.

Precursor mineral	Larmor frequency (MHz)	T (°C)	Phase	$^{[n]}\text{Al}$	$\delta_{\text{iso}}$ (ppm) <sup>a</sup>	$C_q$ (MHz) <sup>b</sup>	$\eta^c$	$\Delta\delta_{\text{iso}}^d$	$^{[n]}\text{Al}$ fraction for each phase (%) <sup>e,*</sup>
Gibbsite	130.28	25	Gibbsite	$^{[6]}\text{Al-1}$	$12.4 \pm 1.0$	$4.5 \pm 0.3$	$0.4 \pm 0.1$	-	$50 \pm 3$
				$^{[6]}\text{Al-2}$	$11.3 \pm 1.0$	$2.3 \pm 0.3$	$0.8 \pm 0.1$	-	$50 \pm 3$
		110	Gibbsite	$^{[6]}\text{Al-1}$	$12.5 \pm 1.0$	$4.5 \pm 0.3$	$0.4 \pm 0.1$	-	$50 \pm 3$
				$^{[6]}\text{Al-2}$	$11.3 \pm 1.0$	$2.3 \pm 0.3$	$0.8 \pm 0.1$	-	$50 \pm 3$
		150	Gibbsite	$^{[6]}\text{Al-1}$	$12.5 \pm 1.0$	$4.5 \pm 0.3$	$0.4 \pm 0.1$	-	$50 \pm 3$
				$^{[6]}\text{Al-2}$	$11.3 \pm 1.0$	$2.3 \pm 0.3$	$0.8 \pm 0.1$	-	$50 \pm 3$
		200	Gibbsite	$^{[6]}\text{Al-1}$	$13.4 \pm 1.0$	$4.6 \pm 0.3$	$0.4 \pm 0.1$	-	$44 \pm 3$
				$^{[6]}\text{Al-2}$	$11.3 \pm 1.0$	$2.3 \pm 0.3$	$0.8 \pm 0.1$	-	$44 \pm 3$
			Boehmite	$^{[6]}\text{Al}$	$11.9 \pm 1.5$	$2.5 \pm 0.3$	-	$7 \pm 1$	$12 \pm 3$
		250	Gibbsite	$^{[6]}\text{Al-1}$	$12.7 \pm 1.0$	$4.5 \pm 0.3$	$0.4 \pm 0.1$	-	$23 \pm 3$
				$^{[6]}\text{Al-2}$	$11.2 \pm 1.0$	$2.4 \pm 0.3$	$0.8 \pm 0.1$	-	$23 \pm 3$
			Boehmite	$^{[6]}\text{Al}$	$10.6 \pm 1.5$	$2.7 \pm 0.3$	-	$5 \pm 1$	$45 \pm 3$
			$\gamma$ -/ $\eta$ - $\text{Al}_2\text{O}_3$	$^{[6]}\text{Al}$	$14.0 \pm 1.5$	$4.6 \pm 0.5$	-	$6 \pm 1$	$7 \pm 2$
				$^{[4]}\text{Al}$	$73.2 \pm 1.5$	$5.5 \pm 0.5$	-	$7 \pm 1$	$2 \pm 1$
		300	Boehmite	$^{[6]}\text{Al}$	$10.6 \pm 1.5$	$2.7 \pm 0.3$	-	$5 \pm 1$	$48 \pm 3$
				$^{[6]}\text{Al}$	$13.8 \pm 1.5$	$4.6 \pm 0.5$	-	$8 \pm 1$	$37 \pm 3$
			$\gamma$ -/ $\eta$ - $\text{Al}_2\text{O}_3$	$^{[4]}\text{Al}$	$73.9 \pm 1.5$	$5.5 \pm 0.5$	-	$9 \pm 1$	$15 \pm 3$

<sup>a</sup>) Isotropic chemical shift

<sup>b</sup>) Quadrupolar coupling constant

<sup>c</sup>) Asymmetry parameter

<sup>d</sup>) Full-width at half maximum of the distribution of the isotropic chemical shift in the Czjzek model

<sup>e</sup>)  $^{[n]}\text{Al}$  fraction for each phase =  $^{[n]}\text{Al}$  for each phase/total area under NMR spectra

\*The uncertainties of each Al site fraction stem from the deviation between experimental and simulated spectra (~1.5%), the contribution from the adjusted NMR parameters (~1.5%), the contribution of spinning sidebands (~1.5%), and phasing of the NMR spectrum (~1.5%). Considering these uncertainties, the total error bar of  $\pm 3\%$  is estimated.



Kim and Lee

## Figures

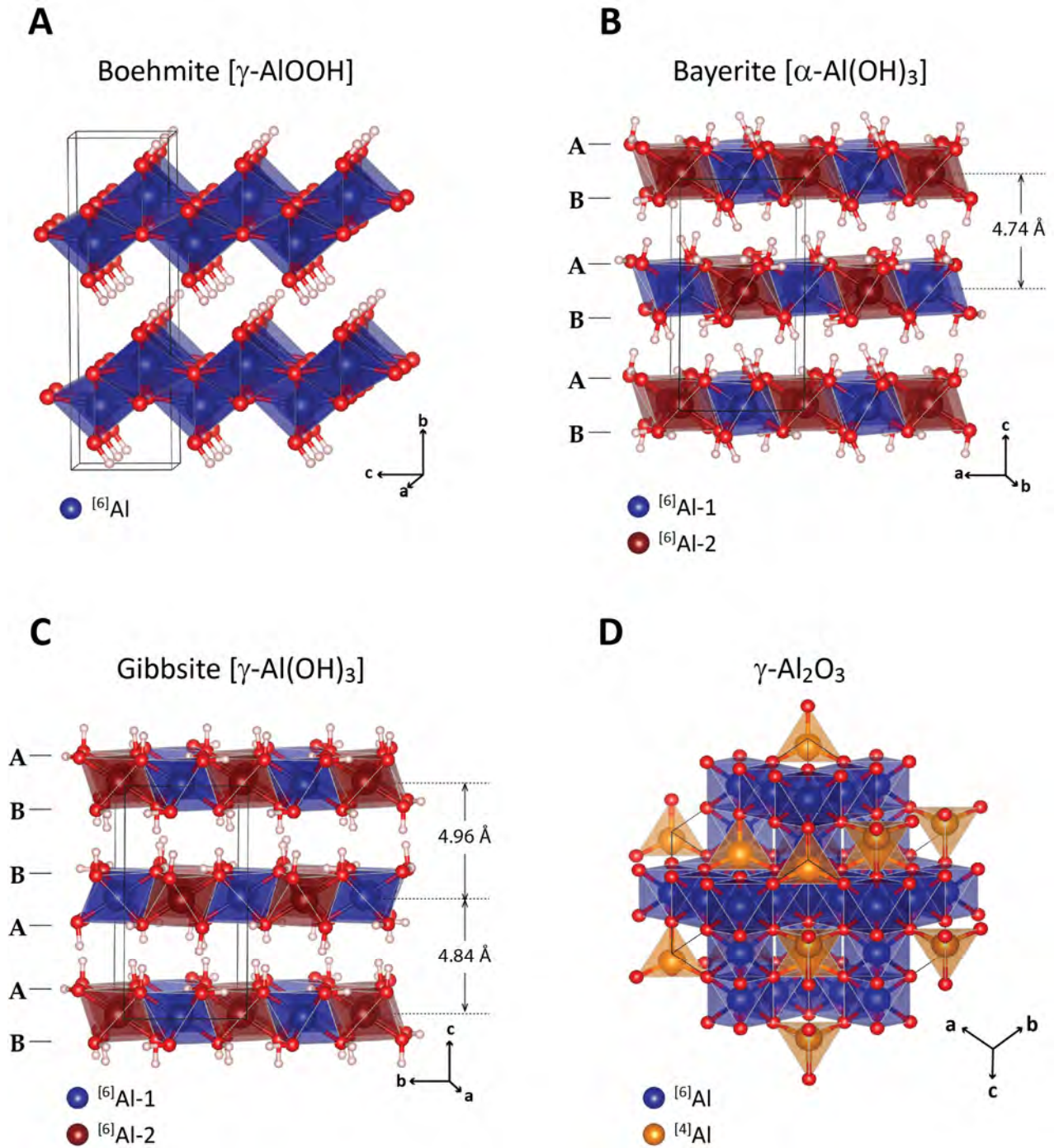


Figure 1.

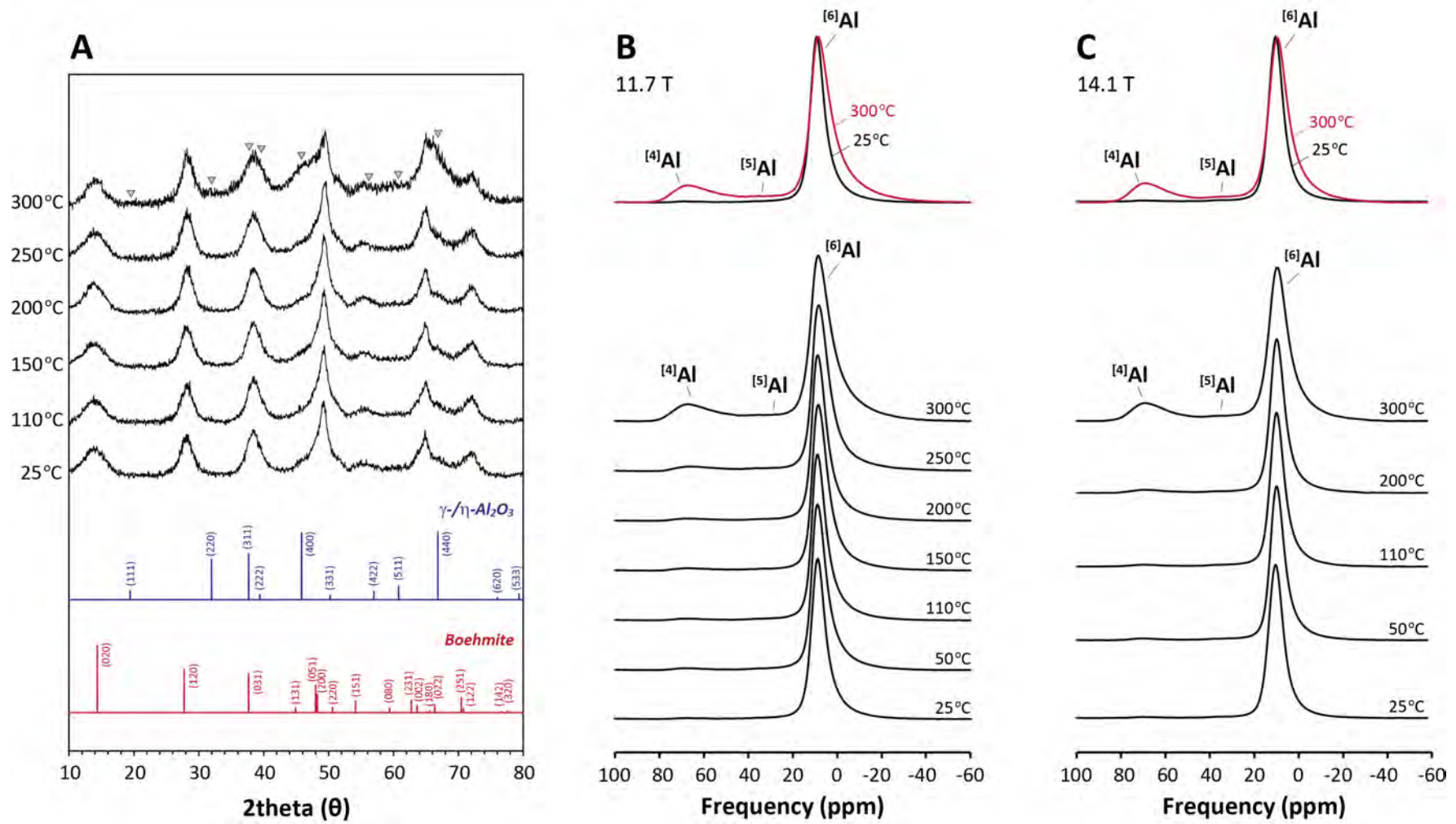


Figure 2.

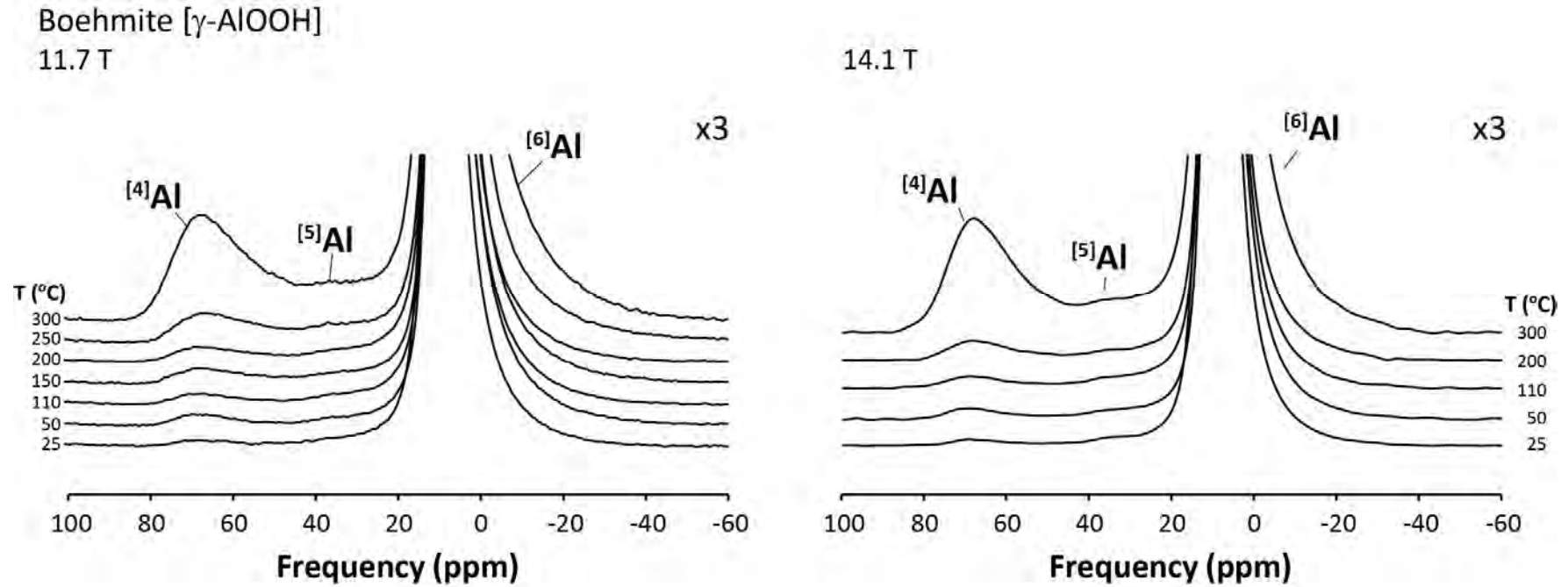


Figure 3.

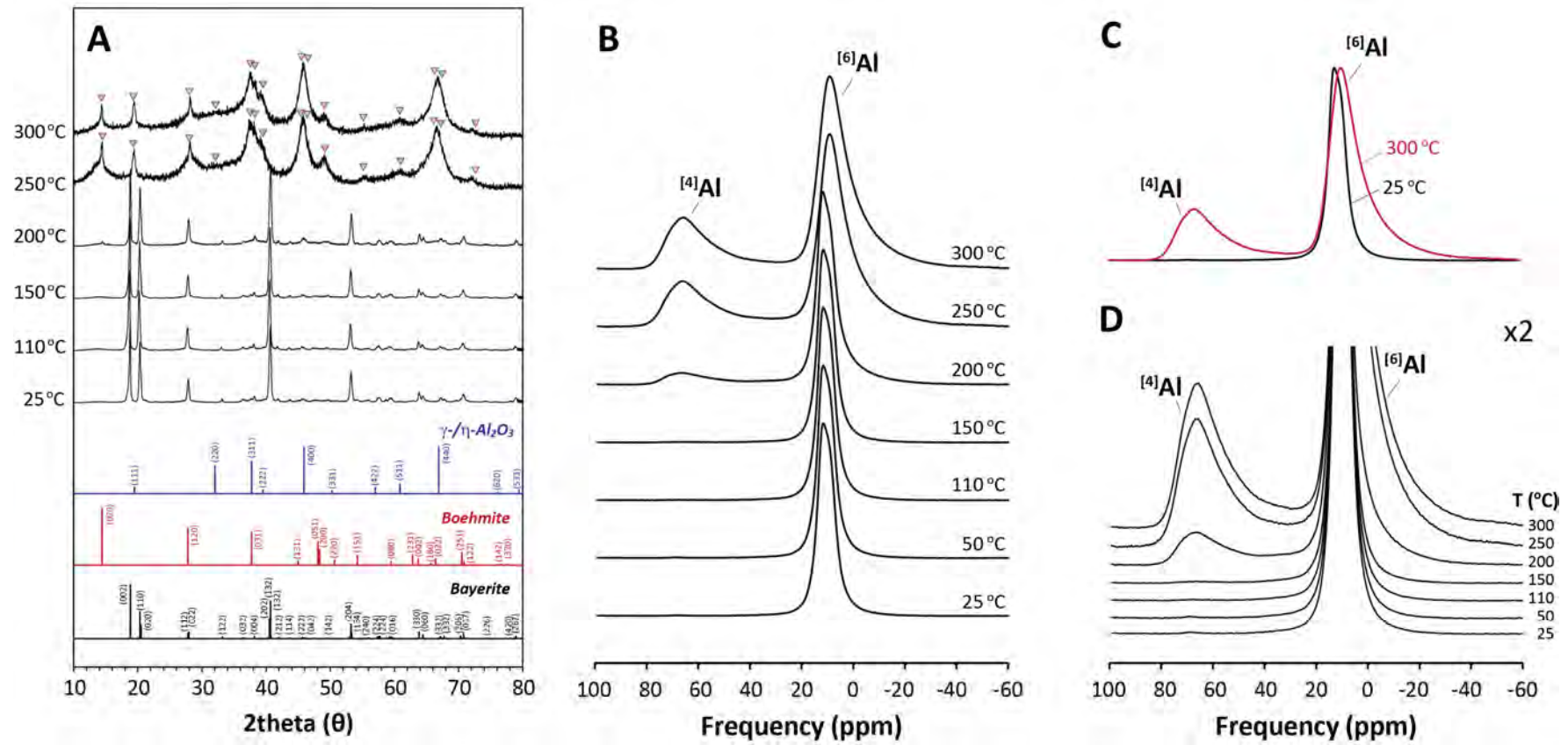


Figure 4.



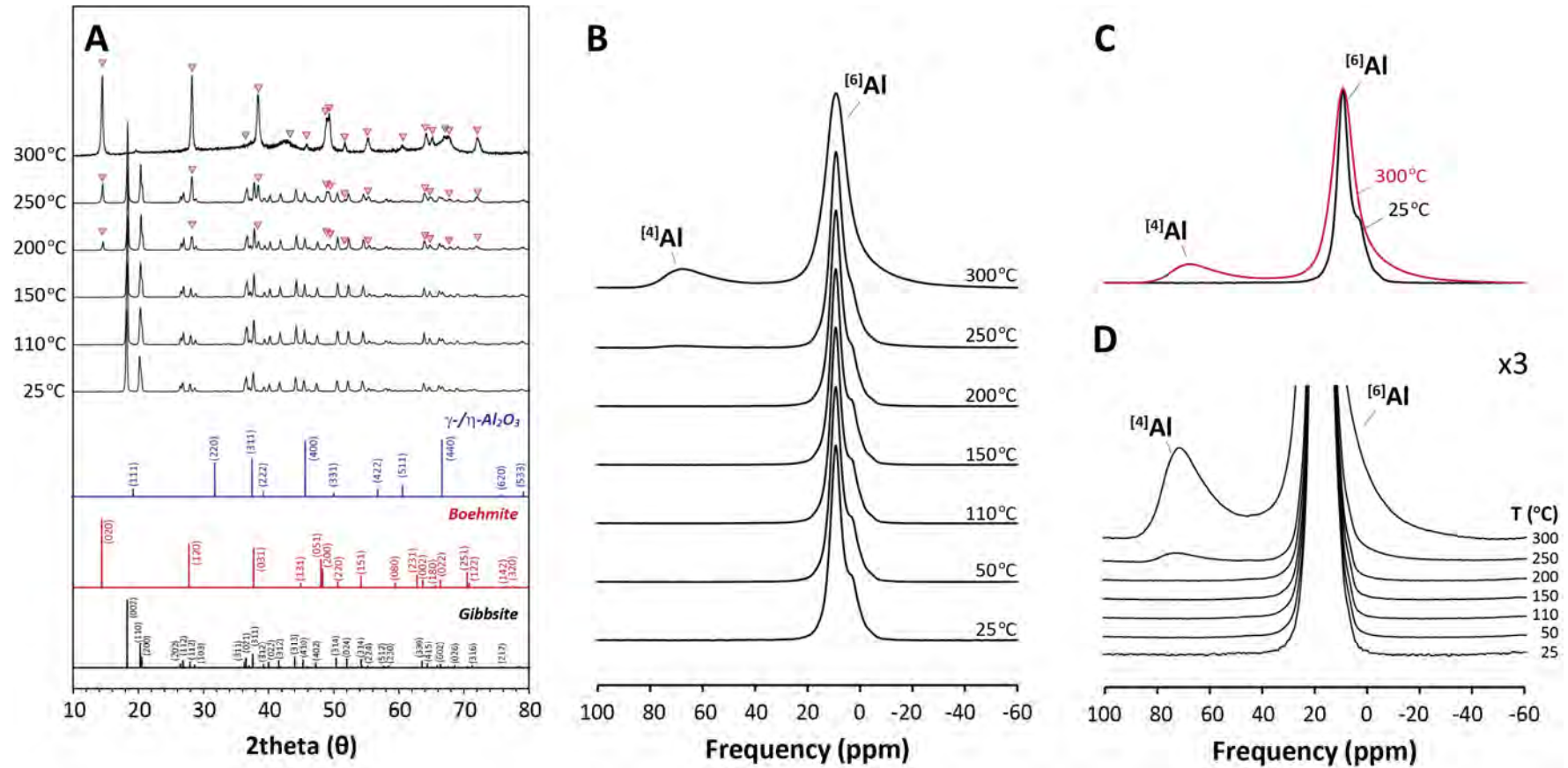


Figure 5.

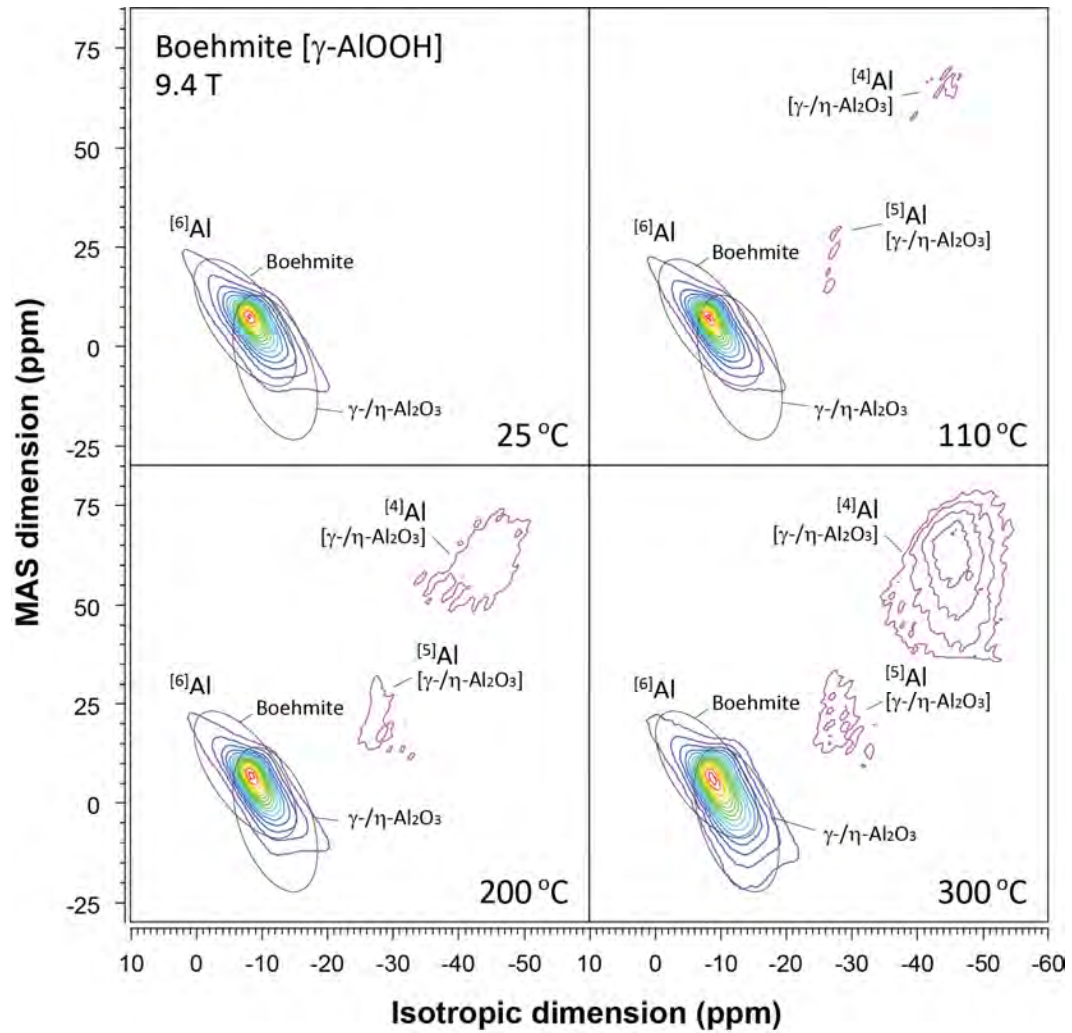


Figure 6.

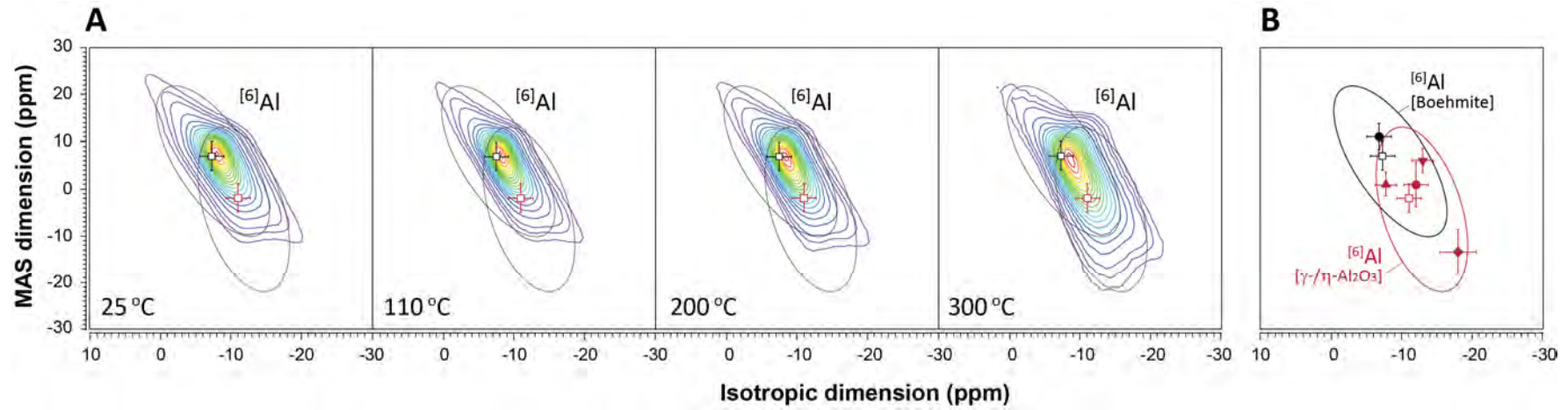


Figure 7.

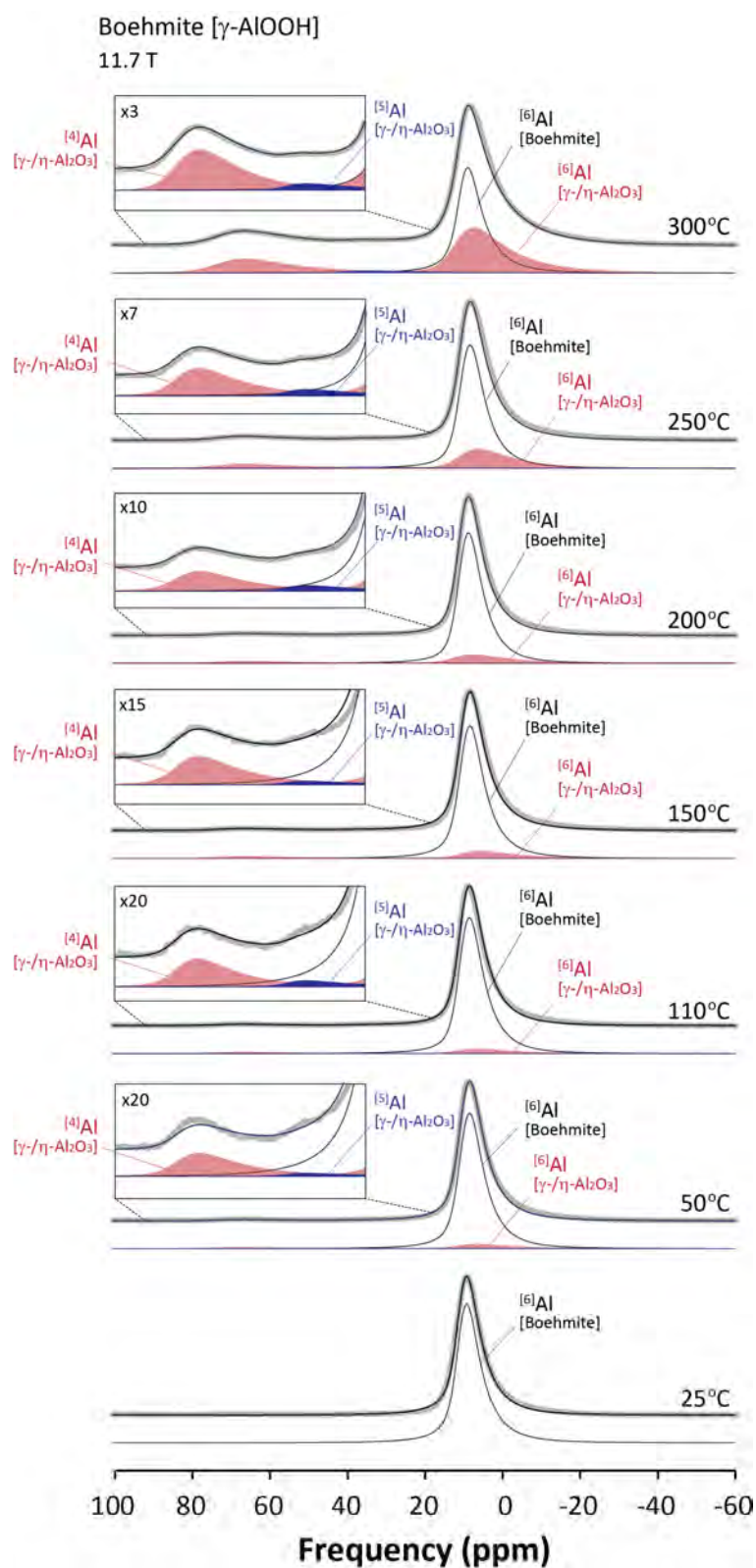


Figure 8.



Kim and Lee

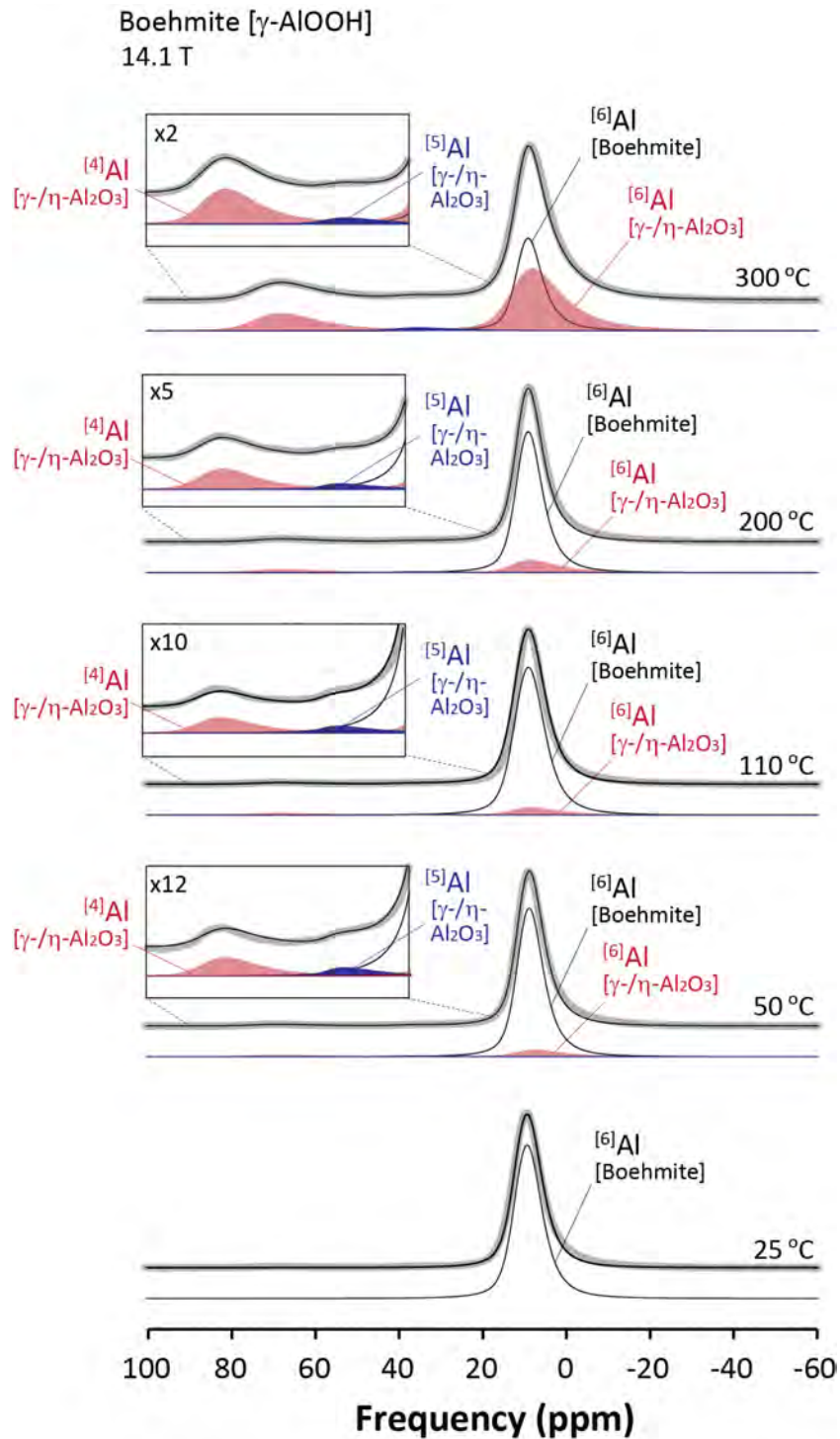


Figure 9.

Kim and Lee

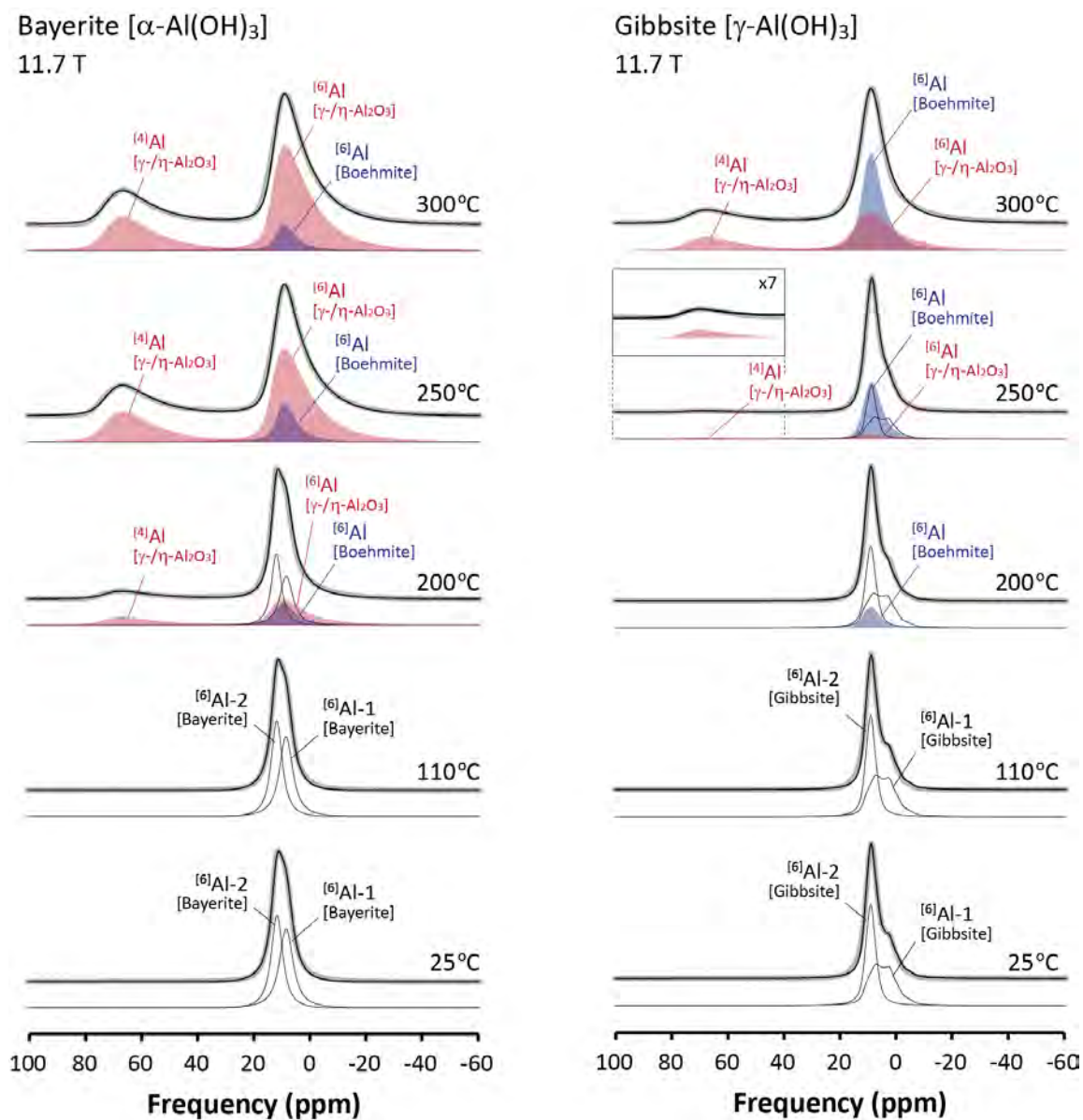


Figure 10.

Kim and Lee

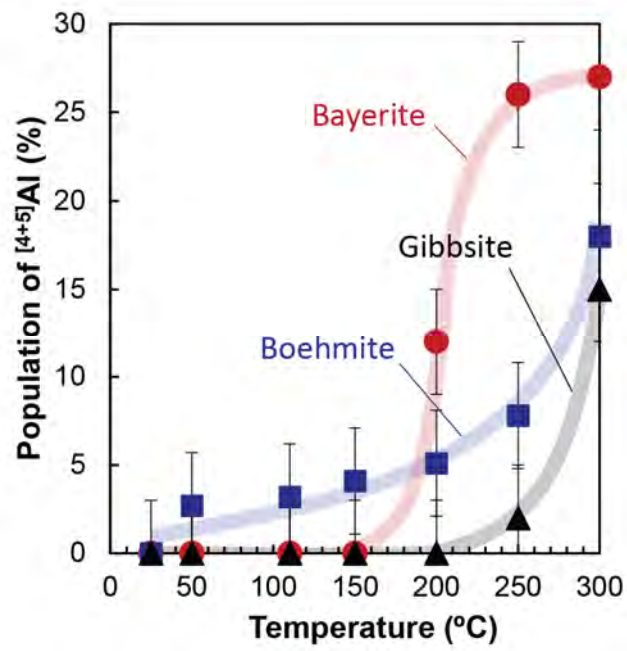


Figure 11.

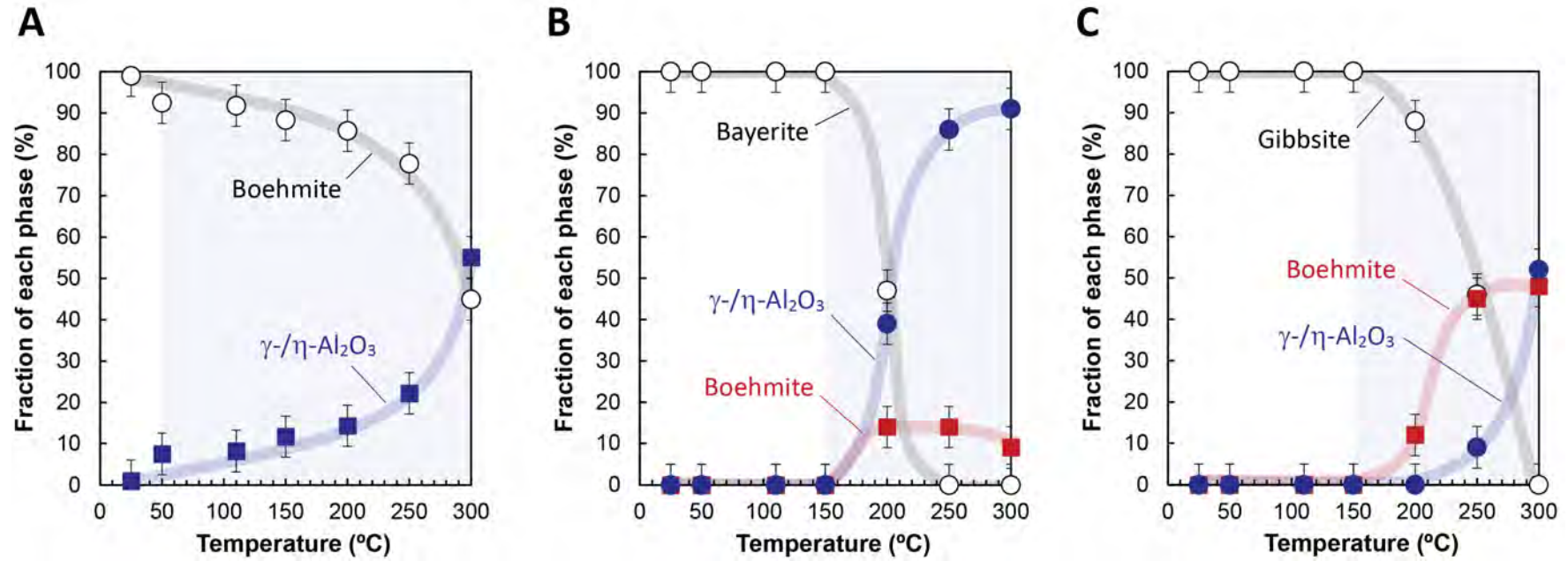


Figure 12.